JGR Solid Earth

RESEARCH ARTICLE
10.1029/2021JB022712

Special Section:
Ophiolites and Oceanic Lithosphere, with a focus on the Samail ophiolite in Oman

Carbon Geochemistry of the Active Serpentinization Site at the Wadi Tayin Massif: Insights From the ICDP Oman Drilling Project: Phase II

Lotta Ternieten[1], Gretchen L. Früh-Green[1], and Stefano M. Bernasconi[1]

[1]Department of Earth Sciences, ETH Zurich, Zurich, Switzerland

Key Points:

- Two carbonate occurrences are observed: localized dolomite, calcite, and aragonite veins and pervasive dispersed carbonates
- Carbonate precipitation in the peridotite occurred in the last 50 kyr at moderate temperatures, post-dating ocean-floor serpentinization
- The oxygen isotope composition of dispersed carbonates indicates precipitation from highly ^{18}O-depleted fossil groundwater

Correspondence to:
L. Ternieten,
lotta.ternieten@gmail.com

Citation:
Ternieten, L., Früh-Green, G. L., & Bernasconi, S. M. (2021). Carbon geochemistry of the active serpentinization site at the Wadi Tayin Massif: Insights from the ICDP Oman Drilling Project: Phase II. *Journal of Geophysical Research: Solid Earth*, *126*, e2021JB022712. https://doi.org/10.1029/2021JB022712

Received 10 JUL 2021
Accepted 26 NOV 2021

Abstract A large part of the hydrated oceanic lithosphere consists of serpentinites exposed in ophiolites. Serpentinites constitute reactive chemical and thermal systems and potentially represent an effective sink for CO_2. Understanding carbonation mechanisms within ophiolites are almost exclusively based on studies of outcrops, which can limit the interpretation of fossil hydrothermal systems. We present stable and radiogenic carbon isotope data that provide insights into the isotopic trends and fluid evolution of peridotite carbonation in ICDP Oman Drilling Project drill holes BA1B (400-m deep) and BA3A (300-m deep). Geochemical investigations of the carbonates in serpentinites indicate formation in the last 50 kyr, implying a distinctly different phase of alteration than the initial oceanic hydration and serpentinization of the Samail Ophiolite. The oldest carbonates (~31 to >50 kyr) are localized calcite, dolomite, and aragonite veins, formed between 26°C and 43°C and related to focused fluid flow. Subsequent pervasive small amounts of dispersed carbonate precipitated in the last 1,000 years. Macroscopic brecciation and veining of the peridotite indicate that carbonation is influenced by tectonic features allowing infiltration of fluids over extended periods and at different structural levels such as along fracture planes and micro-fractures and grain boundaries, causing large-scale hydration of the ophiolite. The formation of dispersed carbonate is related to percolating fluids with $\delta^{18}O$ lower than modern ground and meteoric water. Our study shows that radiocarbon investigations are an essential tool to interpret the carbonation history and that stable oxygen and carbon isotopes alone can result in ambiguous interpretations.

Plain Language Summary Water-rock interactions that have biological and economic importance have received increasing interest in recent years. Carbon species, stored in the atmosphere, biosphere, oceans, and lithosphere, are profoundly affected by biotically and abiotically controlled exchange reactions among these reservoirs. Carbon is an essential element for life and contributes to the greenhouse effect in the form of CO_2 and CH_4. Unraveling water-rock reactions that transform atmospheric CO_2 into thermodynamically stable carbonates helps to better understand long-term carbon storage in the lithosphere and its long-term influence on climate and to better evaluate the potential for life within the lithosphere. This study uses samples recovered by drilling mantle sequences of the Wadi Tayin Massif in Oman and presents chemical data to evaluate carbon sources, speciation, and transformations. The Wadi Tayin Massif is located in the Samail Ophiolite and comprises mantle rocks. Mantle rocks react in contact with water to form serpentine and create an environment that promotes the transformation of CO_2 into carbonates. Our results demonstrate large-scale carbonization of the massif and a dominance of dispersed carbonate formation below the surface. Our study provides insights into the carbon cycle and will help to evaluate the potential of mantle rocks to store carbon and sustain life.

1. Introduction

Serpentinites make up an important component of the hydrated oceanic lithosphere and are commonly exposed on the ocean floor at slow-spreading and ultraslow-spreading ridges and in ophiolites on continents, constituting highly reactive chemical and thermal systems. The alteration of oceanic lithosphere by hydrothermal fluids is the primary driver of hydrosphere-lithosphere volatile exchange and has significant consequences for rock physical properties and planetary-scale element fluxes (Beinlich, John, et al., 2020; Lister, 1972; Wheat & Mottl, 2004). Carbon, as one of the most important elements on Earth, is stored in ultramafic rocks in the form of gaseous CO_2, and CH_4 in fluid inclusions, as solid inorganic carbonate and graphite, and as organic compounds that can be abiotically or biotically produced (Delacour, Früh-Green, Bernasconi, Schaeffer & Kelley, 2008; Kelley & Früh-Green, 2001; McCollom & Seewald, 2006). C-bearing species have multiple origins and can persist in ancient

mantle domains over extended periods. Previous studies have shown that the speciation, concentration, and isotopic composition of carbon provide information about the chemical and physical conditions of the reservoir and the dominant physical, chemical, and/or biological processes in the system (Arai et al., 2012; Charlou et al., 2002; Delacour, Früh-Green, Bernasconi & Kelley, 2008; Kelley et al., 2005; Schwarzenbach, Früh-Green, et al., 2013; Shanks et al., 1995).

Recent studies have shown that microbial life can be sustained within the lithosphere by fluid-mediated chemical reactions that provide utilizable energy resources, which implies that the deep subsurface biosphere may be the largest microbial habitat on Earth (Barry et al., 2019; Colman et al., 2017; Fullerton et al., 2019). For example, hydrothermal circulation of fluids have been postulated to liberate CH_4-rich fluids from intrusive rocks in the oceanic lithosphere (Labidi et al., 2020; Wang et al., 2018), and redox reactions during the formation of serpentine from mantle olivine and pyroxene generate substantial amounts of H_2 (McCollom & Bach, 2009). Production of H_2 by serpentinization has been identified at mid-ocean ridges (Cannat et al., 2010; Kelley et al., 2005; Konn et al., 2015), as well as on-land (Etiope & Sherwood Lollar, 2013) and in the shallow forearc of subduction zones (Mottl et al., 2003; Ohara et al., 2012). Metagenomic studies of serpentinization-fueled hydrothermal deep-sea vents and continental fluid seeps provide evidence for microbial H_2 and CH_4 utilization in these harsh environments where nutrient and electron acceptor availability may be limited by high pH, which in turn depends on the temperature of the system (Brazelton et al., 2012; Curtis et al., 2013; Ohara et al., 2012; Schrenk et al., 2013).

Hydration of mantle peridotites can also be associated with the storage of carbon in large carbonate deposits. Serpentinization at temperatures below ~200°C produces fluids with high Ca^{2+} concentration and high pH, which can lead to carbonate precipitation (Frost & Beard, 2007; Palandri & Reed, 2004). Natural carbon uptake in thermodynamically stable carbonate may represent a means for permanently removing CO_2 from the atmosphere (Kelemen & Matter, 2008) and may help stabilize atmospheric carbon dioxide concentrations over long timescales. The carbon uptake potential is particularly strong in the ultramafic part of the oceanic lithosphere that has previously equilibrated under dry high-temperature conditions and has high concentrations of divalent metal ions required for carbonate mineral formation (Kelemen et al., 2011). The resulting carbonate minerals are typically accompanied by secondary silicates and Fe-oxide, hydroxide, and/or sulfide phases. An extreme endmember of carbonation is listvenite, which forms where extensive infiltration of CO_2-rich fluids alter ultramafic rocks and where almost the entire inventory of Mg and Ca cations are incorporated into carbonate minerals (Halls & Zhao, 1995).

To better evaluate the potential of ultramafic rocks as long-term storage for CO_2, quantitative information on the sources and sinks of carbon is necessary. One critical factor contributing to continuing uncertainty is the difficulty in obtaining samples directly from subsurface environments near mid-ocean ridges. Consequently, most estimates are based on information inferred from analysis of hydrothermal fluids discharged at the seafloor. One possibility to bypass this problem is to study ophiolites. One of the largest and best-explored ophiolite complexes is the Samail Ophiolite in the Sultanate of Oman and the United Arab Emirates, which includes massifs in the south that represent relics of a mid-ocean ridge (Chavagnac et al., 2013; Clark & Fontes, 1990; Coleman, 1977; Coleman & Hopson, 1981; Falk & Kelemen, 2015; Falk et al., 2016; Hanghoj et al., 2010; Hopson et al., 1981; Kelemen & Matter, 2008; Mervine et al., 2014; Nasir et al., 2007; Neal & Stanger, 1983; Paukert et al., 2012; Stanger, 1985; Streit et al., 2012).

The Samail Ophiolite comprises a complete sequence of the oceanic lithosphere from the upper mantle through to the oceanic crust, all of which have recently been the target of comprehensive drilling and subsequent analysis of rock core, logging, hydrological and microbial sampling in the course of the Oman Drilling Project (OmanDP) (Kelemen et al., 2020). We present petrographic and carbon and oxygen isotope analyses from Holes BA1B and BA3A of the OmanDP. Serpentinized dunites and harzburgites that are variably carbonated were recovered to better constrain the conditions and reaction pathways driving alteration and carbonation at a large scale. Mineralogy, isotopic trends, carbon sources, and speciation are discussed to constrain critical reaction parameters and chemical equilibration during natural large-scale hydration and carbonization. In addition, our study aims to characterize biogenic and abiogenic processes controlling carbon cycling within the Samail Ophiolite and evaluate the potential for long-term storage for CO_2.

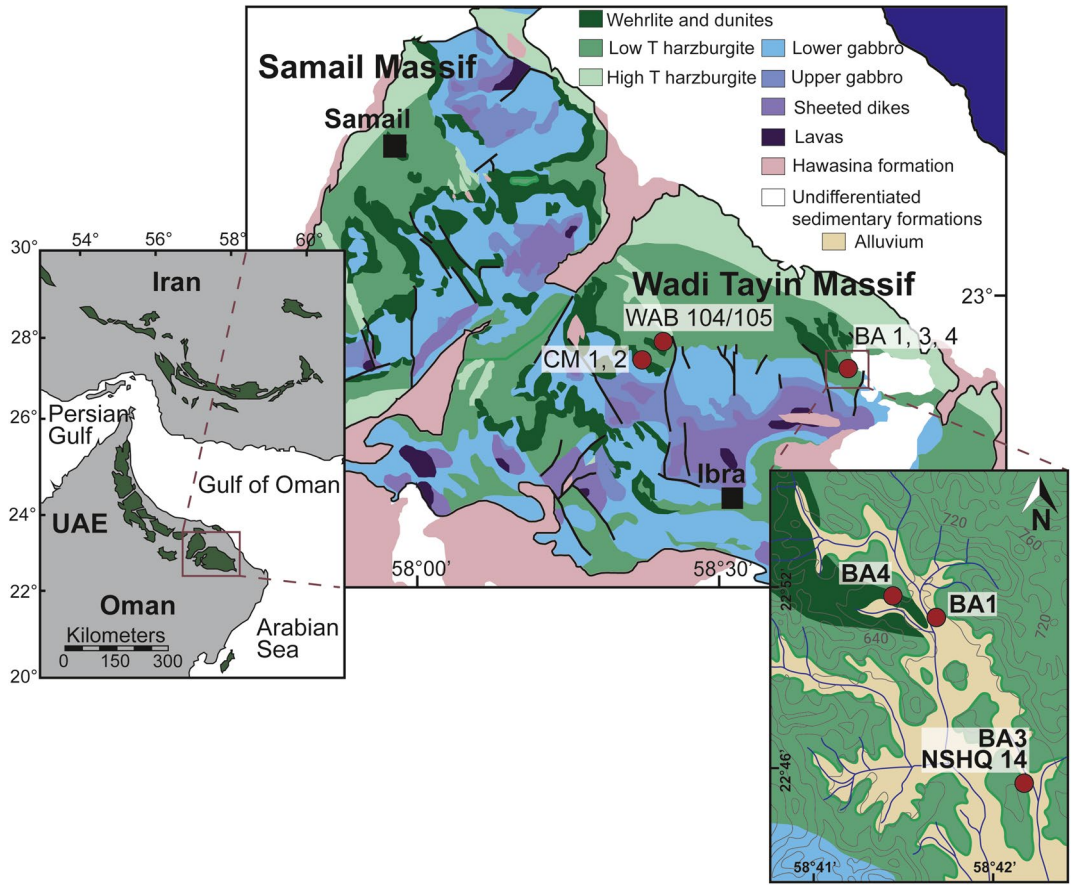

Figure 1. Geological map of the Samail and Wadi Tayin Massifs, Samail ophiolite, modified after Hanghoj et al. (2010) and Nicolas et al. (2000) with locations of the BA drill sites (active serpentinization), modified after Kelemen et al. (2020). Also shown are the locations of the CM (crust-mantle boundary) site of the Oman Drilling Project (Kelemen et al., 2020) and the location of the drilled wells WAB 104, WAB 105 (Nothaft, Templeton, Rhim, et al., 2021), and NSHQ 14 (Miller et al., 2016) (red circles).

2. Geological Setting and Sampling

The Samail Ophiolite consists of ~15 massifs and is the most extensive and best-exposed cross-section through the oceanic lithosphere (Figure 1). The ophiolite comprises an intact stratigraphy of Penrose-type layered oceanic crust and mantle composed of pelagic allochthonous sediments, overlying pillow basalts, a sheeted dike complex, gabbros, and upper mantle peridotite (Coleman, 1981; Searle & Malpas, 1980). The metamorphic sole underneath the ophiolite sequence consists of metaphyllites, greenschist facies metabasalts, and minor amphibolites of the Haybi Complex (Searle & Malpas, 1980). The metamorphic sole is underlain by Permian to Late Cretaceous pelagic sediments, meta-volcanic rocks, and shelf-facies limestone of the Hawasina Group, which appear as tectonic windows between the ophiolitic massifs (Figure 1, Braun & Kelemen, 2002; Coleman, 1981; Nasir et al., 2007; Searle et al., 2015; Stanger, 1985).

The oceanic lithosphere formed most likely at a medium-spreading to fast-spreading ridge like the East Pacific Rise (EPR) or the Juan de Fuca Ridge (Nicolas, 1989; Tilton et al., 1981). U-Pb dating of magmatic zircon and $^{40}Ar/^{39}Ar$ ages of mica and hornblende from the metamorphic sole indicates that thrusting of the Samail Ophiolite onto the autochtonous Proterozoic to Mesozoic sedimentary Arabian continental margin occurred between 95 and 71 Myr (Cowan et al., 2014; Gnos, 1998; Hacker, 1994; Hacker & Gnos, 1997; Hacker & Mosenfelder, 1996; Hacker et al., 1996; Lanphere, 1981; Rabu et al., 1993; Rioux et al., 2012, 2013, 2016; Tilton et al., 1981; Warren et al., 2005). During this time, the ophiolite was repeatedly under shallow seawater or emerged above sea level caused by oscillating transgression-regression cycles (Coleman, 1981).

2.1. Samail and Wadi Tayin Massif

The southern massifs of the Oman ophiolite complex, known as the Samail and Wadi Tayin Massifs, were formed primarily via a MORB-like, single-stage process at a submarine spreading ridge (Godard et al., 2003). Outcrops of the crustal and mantle sequence can be found at both massifs; however, the structural thickness of the mantle section differs between the Samail and the Wadi Tayin Massif with 4 km and over 10 km, respectively (Hanghoj et al., 2010; Nicolas et al., 2000). The extensive mantle sequence at the Wadi Tayin Massif is overlain by a 5–7-km-thick gabbroic crustal section, sheeted dikes, and pillow lavas (Figure 1). The mantle section of the southern massifs comprises mainly harzburgite and minor lherzolite that host 5%–15% dunites and contains multiple mafic intrusions (Boudier & Coleman, 1981; Pallister & Knight, 1981).

The harzburgites record "near fractional" partial melt extraction and are geochemically similar to abyssal peridotites (Godard et al., 2000; Kelemen et al., 1995; Le Mée et al., 2004; Monnier et al., 2006). Dunites represent channels of focused melt transport through the harzburgites, with a thickness of <1 cm–100 m or more, and were formed by melt-rock interaction between MORB-like melts and harzburgite (Braun, 2004; Braun & Kelemen, 2002; Kelemen et al., 1995). Gravity anomalies (Ravaut et al., 1997) suggest that the Samail and Wadi Tayin Massifs are composed of 30%–60% (locally reaching 100%, Falk & Kelemen, 2015; de Obeso & Kelemen, 2018) serpentinized mantle peridotite, extending up to 5 km below the present-day surface. In addition, listvenites are observed at the base of the ophiolitic mantle section and are formed at high temperatures during subduction by the reaction with CO_2-rich, sediment-derived fluids (Beinlich, Plümper, et al., 2020; Falk & Kelemen, 2015). However, there is still debate whether the southern massifs were formed at a "normal" mid-ocean ridge (Braun, 2004), in a supra-subduction zone setting, or via unique processes during ophiolite obduction (Hanghoj et al., 2010; Kelemen et al., 2020). For instance, there are some differences compared to typical spreading ridges, such as slightly high Th/Nb and SiO_2 in some lavas (Hanghoj et al., 2010) and higher spinel Cr-number in some peridotites (Dick & Bullen, 1984) of the Wadi Tayin Massif.

Tectonic uplift and erosion of the southern massif mantle rocks lead to extensive ongoing serpentinization of the peridotite by groundwaters (Kelemen et al., 2011; Kelemen & Matter, 2008; Paukert et al., 2012). The reaction of groundwaters with peridotite at low temperatures forms (a) medium pH ~8, Mg-HCO_3-rich, oxidized fluids in the near-surface (defined as Type I fluids by Barnes and O'Neil, 1969, Bruni et al., 2002, Dewandel et al., 2005). When isolated from the atmosphere at greater depth, (b) high pH ~12, Ca-OH-rich, highly reduced fluids with no dissolved carbon or Mg^{2+} (Type II fluids) are formed (Neal & Stanger, 1985). These fluids mixed with dissolved inorganic carbon (DIC: $CO_{2(aq)} + HCO_3^- + CO_3^{2-}$) or in contact with atmospheric $CO_{2(g)}$ can lead to a large volume of carbonates. Previous studies showed that travertine and vein formation occurred between 20°C and 60°C and that their ^{14}C ages ranged from modern to >50 kyr with an average of about 26 kyr (Clark & Fontes, 1990; Kelemen & Matter, 2008; Kelemen et al., 2011; Streit et al., 2012).

2.2. The Oman Drilling Project: Phase II

Phase II of the OmanDP drilled nine boreholes (from 300 m to a maximum of 400 m deep) at two sites in the Wadi Tayin Massif and targeted the crust-mantle transition zone (CM) and an active alteration zone (BA) in mantle peridotites (Figure 1). The OmanDP aimed to establish a multi-borehole observatory (MBO) to address a spectrum of questions that connect the deep mantle and the ancient ocean floor with modern hydrology and ongoing biogeochemical reactions in the mountains and wadis of the Samail Ophiolite. Our study focuses on the active alteration Site BA, which targets hydration and carbonization at temperatures <50°C and provides an excellent opportunity to better understand how alteration and serpentinization are coupled to the carbon cycle.

Drilling at Site BA included three diamond cores (BA3A, BA1B, and BA4A) and two rotary drill holes (BA1C and BA1D). Drill cores of the OmanDP–Phase II are described in detail in Kelemen et al. (2020). We focus on the two Holes BA1B and BA3A from the mantle section of the ophiolite. The cores had 100% recovery; in BA1B, they consist of ~55% harzburgite, ~35% dunite, and ~10% mafic dykes and alluvium. In BA3A, ~97% harzburgite and less than 3% mafic dykes and alluvium were recovered (Figure 2). The ultramafic rocks from Site BA reveal a high and heterogeneous degree of serpentinization, several pyroxenite and gabbroic dykes, in parts extended oxidation zones, and local rodingitization (Kelemen et al., 2020). Contacts between ultramafic and mafic domains are marked by chlorite, prehnite, talc, and hydrogrossular, indicating metasomatism on a millimeter scale. A recent *in situ* oxygen isotope study of the serpentinites from Hole BA1B defined three distinct stages of

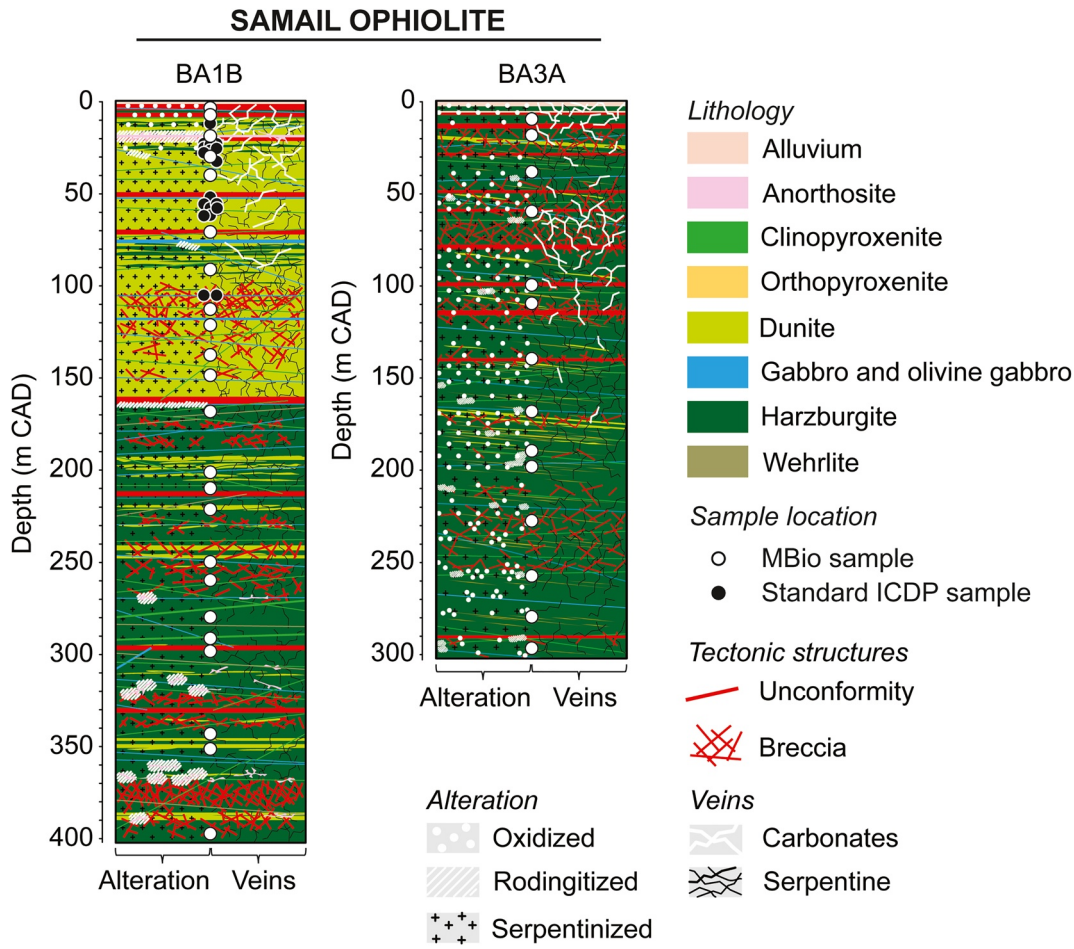

Figure 2. Simplified downhole logs (meters Chikyu Adjusted Depth = m CAD) of the dominant lithologies and tectonic features recovered in Holes BA1B and BA3A of the OmanDP containing serpentinized peridotites. BA1B consists of 160 m of dunite on top, followed by 240 m of harzburgite. BA3A contains 300 m of harzburgite. Both holes are cut by multiple gabbroic intrusions (modified after Kelemen et al., 2020). The white dots indicate locations of microbiological (MBio) samples, and the black dots indicate locations of standard ICDP samples (sampled under non-sterile conditions).

hydration (Scicchitano et al., 2020): (a) seafloor serpentinization at temperatures of up to ~190°C, followed by (b) serpentinization caused by infiltration of meteoric water with $\delta^{18}O$ value of ~−7‰ at 32°C, and (c) ongoing serpentinization also at 30°C–33°C by ground and/or meteoric water with $\delta^{18}O$ value of ~−0.7‰. Carbonate-rich zones occur in the upper 150 m and are characterized by a distinct decrease in vein abundance with depth.

3. Materials and Methods

Isotopic investigations were made on 26 harzburgites and 9 dunites from Holes BA1B and BA3A, covering the diversity of rock types and alteration. In addition, we measured clumped isotopes on 21 carbonate veins from 19 serpentinized peridotites. Petrographic investigations were made on 20 doubly polished thin sections of representative samples from Hole BA1B. Detailed information on the samples is given in Tables 1 and 2. A simplified lithostratigraphy is shown in Figure 2. Samples are named after ICDP guidelines: Expedition_Site, Hole (Chikyu Hole)_Core, Coretype_Section_Interval in cm (e.g., 5057_BA1B (5B)_75Z_1_39–90). For simplicity, we have removed the expedition number "5057," which is the same for all samples, and the Chikyu Hole information (the example above is thus reported as BA1B_75Z_1_39–90). The depth below the present-day surface is given in meters and defined as the Chikyu Adjusted Depth (CAD). Details of the depth computations are given in Kelemen et al. (2020), Methods, and explanatory notes.

Table 1
Content and Carbon (VPDB) and Oxygen (VPDB) Isotope Compositions in Total Carbon (TC), Total Non-Carbonate Carbon (NCC), and Total Inorganic Carbon (TIC) and Estimated Carbonate Formation Temperature of Whole-Rock MBio Samples From the Wadi Tayin Massif at the Samail Ophiolite

Site	Hole	Core	Section	Interval (cm) Top	Interval (cm) Bot.	Depth (m CAD) Top	Depth (m CAD) Bot.	Lithology	TC (ppm)	NCC (ppm)	TIC[a] (ppm)	$\delta^{13}C_{TC}$ (‰)	$\delta^{13}C_{NCC}$ (‰)	$\delta^{13}C_{TIC}$ (‰)	$\delta^{18}O_{TIC}$ (‰)	T[b] (°C)	
BA	1B	2	2	27	35	3.52	3.60	Serpentinized harzburgite	1,300	165	1,134	−9.47	−25.87	−9.74	−1.99	9	59
BA	1B	3	2	73	85	7.34	7.46	Serpentinized dunite	13,608	139	13,468	−12.02	−26.14	−12.07	−2.82	13	65
BA	1B	7	2	21	63	18.81	19.23	Serpentinized dunite	296	182	114	−10.43	−26.59	−7.57	−13.51	72	167
BA	1B	11	1	6	33	29.76	30.03	Serpentinized dunite	1,619	136	1,483	−10.59	−24.10	−10.90	−11.25	57	137
BA	1B	20	3	0	50	40.14	40.64	Serpentinized dunite	1,489	222	1,267	−8.85	−25.64	−11.55	−15.80	88	204
BA	1B	31	4	0	53	70.85	71.38	Serpentinized harzburgite	736	207	529	−9.18	−26.12	−9.75	−11.50	59	140
BA	1B	38	2	0	50	90.52	91.02	Serpentinized dunite	399	196	203	−11.52	−27.04	−13.07	−11.94	62	146
BA	1B	45	4	0	49	113.15	113.64	Serpentinized dunite	786	175	611	−8.57	−26.60	−8.02	−14.29	77	178
BA	1B	48	2	11	60	120.68	121.17	Serpentinized dunite	1,011	263	748	−9.00	−26.17	−11.72	−14.51	79	182
BA	1B	54	2	0	49	138.36	138.85	Serpentinized dunite	569	191	378	−10.65	−26.48	−12.51	−11.92	62	146
BA	1B	57	3	0	50	148.53	149.03	Serpentinized dunite	844	221	623	−9.77	−21.61	−13.36	−14.05	76	175
BA	1B	64	3	0	50	169.41	169.91	Serpentinized harzburgite	651	191	460	−12.55	−27.81	−15.02	−14.58	79	183
BA	1B	75	1	39	90	201.09	201.60	Serpentinized harzburgite	1,032	297	735	−11.37	−29.64	−11.17	−13.96	75	173
BA	1B	78	1	48	96	210.18	210.66	Serpentinized harzburgite	918	206	712	−7.24	−26.27	−9.95	−14.48	79	181
BA	1B	81	4	0	51	221.05	221.56	Serpentinized harzburgite	590	238	352	−11.05	−27.37	−11.07	−14.68	80	185
BA	1B	91	3	0	52	250.18	250.70	Serpentinized harzburgite	511	299	212	−14.23	−27.91	−11.69	−14.45	78	181
BA	1B	94	4	0	53	259.99	260.52	Serpentinized harzburgite	750	358	393	−15.90	−28.94	−14.37	−14.71	80	185
BA	1B	101	2	21	76	279.97	280.52	Serpentinized harzburgite	467	200	267	−10.97	−25.73	−10.56	−14.37	78	180
BA	1B	105	1	10	57	290.80	291.27	Serpentinized harzburgite	542	286	256	−9.23	−25.74	−8.26	−14.80	81	187
BA	1B	107	4	0	55	299.04	299.59	Serpentinized harzburgite	721	245	477	−9.57	−24.90	−11.24	−13.68	73	169
BA	1B	122	2	0	50	342.51	343.01	Serpentinized harzburgite	750	265	486	−8.78	−27.98	−9.80	−13.94	75	173
BA	1B	125	1	47	97	351.17	351.67	Serpentinized harzburgite	593	126	467	−9.15	−27.06	−10.66	−13.58	72	168
BA	1B	141	4	0	53	398.04	398.57	Serpentinized harzburgite	723	337	386	−11.18	−26.88	−9.77	−14.55	79	183
BA	3A	7	2	0	35	9.58	9.93	Serpentinized harzburgite	1,241	218	1,022	−7.17	−22.07	−9.09	−11.53	59	141
BA	3A	12	2	32	85	18.87	19.40	Serpentinized harzburgite	1,220	239	981	−8.89	−24.04	−5.90	−14.85	81	188
BA	3A	19	2	0	55	39.25	39.80	Serpentinized harzburgite	752	300	452	−6.30	−24.06	−12.79	−12.91	68	158
BA	3A	27	1	28	88	59.98	60.58	Serpentinized harzburgite	1,242	349	893	−7.98	−23.79	−5.94	−12.34	64	151

Table 1
Continued

Site	Hole	Core	Section	Interval (cm) Top	Interval (cm) Bot.	Depth (m CAD) Top	Depth (m CAD) Bot.	Lithology	TC (ppm)	NCC (ppm)	TIC[a] (ppm)	$\delta^{13}C_{TC}$ (‰)	$\delta^{13}C_{NCC}$ (‰)	$\delta^{13}C_{TIC}$ (‰)	$\delta^{18}O_{TIC}$ (‰)	T[b] (°C)	
BA	3A	43	2	32	83	99.66	100.17	Serpentinized harzburgite	738	170	568	−5.78	−27.99	−4.67	−11.61	60	142
BA	3A	46	3	39	86	109.78	110.25	Serpentinized harzburgite	1,232	473	759	−6.15	−25.94	−6.05	−12.12	63	148
BA	3A	58	3	38	95	139.71	140.28	Serpentinized harzburgite	1,052	206	846	−7.26	−26.14	−7.01	−12.88	68	158
BA	3A	69	3	25	77	169.41	169.93	Serpentinized harzburgite	906	137	769	−9.10	−25.88	−8.47	−11.97	62	146
BA	3A	76	3	0	50	190.41	190.91	Serpentinized harzburgite	1,175	479	696	−8.15	−27.24	−8.45	−13.29	71	164
BA	3A	79	2	41	93	199.04	199.56	Serpentinized harzburgite	215	158	57	−8.77	−25.55	−6.60	−15.12	83	192
BA	3A	89	1	36	85	228.06	228.55	Serpentinized harzburgite	1,131	429	702	−9.33	−27.28	−10.79	−13.80	74	171
BA	3A	99	1	24	76	257.94	258.46	Serpentinized harzburgite	1,100	214	886	−9.00	−24.14	−9.55	−12.62	66	155
BA	3A	106	2	0	50	279.58	280.08	Serpentinized harzburgite	1,084	235	849	−9.54	−25.36	−10.99	−14.21	77	177
BA	3A	113	2	0	49	297.25	297.74	Serpentinized harzburgite	971	332	638	−7.89	−27.32	−6.81	−14.13	76	176

[a]Calculated inorganic carbon content. [b]Range of calculated oxygen isotope temperatures.

3.1. Sample Preparation

Sample preparation depended on whether the samples were aliquots of samples used for microbiological studies and were collected under sterile conditions (denoted as MBio samples) or whether the samples were obtained using standard ICDP protocols (denoted as standard ICDP samples). MBio samples were used for whole-rock analyses, and standard ICDP samples were used to analyze carbonate veins and for petrographic studies. In the field, the MBio dedicated cores were washed on the outside with ultraclean deionized water and cut using a diamond blade saw lubricated with deionized water. For subsampling, the subcore was transferred onto pre-combusted aluminum foil and crushed using an ethanol-washed hammer, chisel, and tweezers. Finally, the MBio subsamples were transferred into an N_2 glovebox, washed two times with N_2-purged deionized water, wrapped in aluminum foil, sealed into mylar bags flushed with N_2 together with an O_2-scrubbing sachet (BD GasPak 260001), and stored at 4°C. A description of sample handling procedures during the OmanDP can be found in the OmanDP Methods and explanatory notes in Kelemen et al. (2020) and Templeton et al. (2021). In our laboratory, the MBio samples (rock chips or core pieces) were cleaned first by ultrasonication in 100 ml dichloromethane (DCM) for 5 min at room temperature and subsequently dried for 24 h at room temperature in a pre-combusted glass container covered with combusted aluminum foil. The rock chips were then crushed, centerpieces collected and ground by hand using an agate mortar cleaned with DCM to obtain a homogenous powder.

We conducted whole-rock analyses of MBio samples to determine concentrations of total carbon (TC), total inorganic carbon (TIC), and total non-carbonate carbon (NCC), and the isotopic compositions ($\delta^{13}C$ and $\delta^{18}O$) of TIC, total carbon ($\delta^{13}C_{TC}$), and total non-carbonate (acid-insoluble) carbon ($\delta^{13}C_{NCC}$). TIC represents all inorganic carbon from a whole-rock powder (including potential carbonate veins) that reacts at room temperature within 24 hr with 6M hydrochloric acid (HCl). Total NCC represents all remaining acid-insoluble carbon phases, including organic compounds, amorphous carbon, and graphite; this carbon fraction is commonly reported collectively as total organic carbon (TOC) (e.g., Delacour, Früh-Green, Bernasconi, Schaeffer & Kelley, 2008). The NCC and $\delta^{13}C_{NCC}$ were determined on 200 mg aliquots decarbonated with 3 ml of 6M hydrochloric acid (HCl). The remaining material was rinsed several times with Milli-Q water, dried at 70°C overnight, and re-homogenized by hand using an agate mortar.

Journal of Geophysical Research: Solid Earth

10.1029/2021JB022712

Table 2

Carbon and Oxygen Isotope Composition (VPDB), Carbonate Clumped Isotope Compositions (CDES), Estimated Formation Temperatures, and Fluid Equilibrium Oxygen Isotope Compositions (VSMOW) of Carbonate Veins in Ultramafic Rocks From the Wadi Tayin Massif at the Samail Ophiolite

				Interval (cm)		Depth (m CAD)					$\delta^{13}C_{TIC}$		$\delta^{18}O_{TIC}$		$\Delta 47$		T		$\delta^{18}O_{Fluid}$[b]
Site	Hole	Core	Section	Top	Bot.	Top	Bot.	Lithology	Mineral	n	(‰)	σ	(‰)	σ	(‰)	σ	(°C)	68% CL[a]	(‰)
BA	1B	4	4	12	17	11.15	11.20	Serpentinized harzburgite	Aragonite	9	−10.61	0.02	−3.74	0.05	0.646	0.041	34	5	−0.40
BA	1B	4	4	12	17	11.15	11.20	Serpentinized harzburgite	Aragonite	9	−9.38	0.02	−5.12	0.06	0.639	0.023	36	3	−1.47
BA	1B	8	4	34	35	23.28	23.29	Serpentinized dunite	Aragonite	8	−9.48	0.03	−3.47	0.06	0.659	0.009	29	1	−1.09
BA	1B	8	4	34	35	23.28	23.29	Serpentinized dunite	Aragonite	9	−9.21	0.03	−3.55	0.04	0.662	0.020	28	2	−1.29
BA	1B	14	1	59	62	23.29	23.32	Serpentinized dunite	Dolomite	8	−11.70	0.03	−1.29	0.10	0.617	0.016	29	2	−1.34
BA	1B	8	4	61	66	23.55	23.60	Serpentinized dunite	Dolomite	9	−10.13	0.06	−3.85	0.06	0.580	0.047	43	7	−1.03
BA	1B	14	3	0	20	24.58	24.78	Serpentinized dunite	Aragonite	9	−9.64	0.05	−3.90	0.07	0.665	0.024	27	3	−1.81
BA	1B	14	3	81	84	25.39	25.42	Serpentinized dunite	Aragonite	8	−11.20	0.04	−2.92	0.04	0.664	0.023	28	3	−0.79
BA	1B	9	4	19	20	26.28	26.29	Serpentinized dunite	Aragonite	10	−10.17	0.02	−3.53	0.04	0.662	0.030	28	3	−1.24
BA	1B	10	3	4	6	28.66	28.68	Serpentinized dunite	Aragonite	8	−9.32	0.04	−3.66	0.08	0.630	0.031	39	4	0.61
BA	1B	17	1	17	22	32.87	32.92	Gabbro	Aragonite	10	−11.46	0.11	−3.79	0.13	0.670	0.012	26	1	−2.03
BA	1B	17	1	17	22	32.87	32.92	Gabbro	Aragonite	7	−11.27	0.01	−3.55	0.05	0.648	0.025	33	3	−0.44
BA	1B	25	2	8	16	51.68	51.76	Serpentinized dunite	Calcite	10	−13.94	0.01	−2.15	0.03	0.660	0.033	29	3	0.80
BA	1B	26	4	84	89	56.79	56.84	Serpentinized dunite	Calcite	9	−15.46	0.02	−2.27	0.03	0.650	0.039	32	4	1.29
BA	1B	26	4	79	83	56.74	56.78	Serpentinized dunite	Calcite	11	−14.42	0.01	−2.45	0.03	0.657	0.038	30	4	0.68
BA	1B	27	2	78	81	58.38	58.41	Serpentinized dunite	Calcite	11	−14.75	0.02	−3.50	0.04	0.657	0.024	30	2	−0.43
BA	1B	27	3	13	17	58.62	58.66	Serpentinized dunite	Calcite	12	−15.49	0.03	−3.26	0.08	0.664	0.030	28	3	−0.63
BA	1B	28	2	77	82	61.38	61.43	Serpentinized dunite	Calcite	9	−23.18	0.30	−4.49	0.06	0.634	0.016	37	2	−0.06
BA	1B	28	2	68	72	61.29	61.33	Serpentinized dunite	Calcite	8	−23.99	0.07	−4.77	0.02	0.656	0.016	30	2	−1.69
BA	1B	43	1	33	41	105.03	105.11	Olivine Gabbro	Calcite	7	4.44	0.06	−3.20	0.03	0.644	0.025	34	3	0.66
BA	1B	43	2	29	31	105.80	105.82	Serpentinized dunite	Calcite	9	6.87	0.12	−3.53	0.02	0.631	0.036	39	4	1.22

Note. n number of replicate measurements.

[a]Confidence Level (CL). [b]Calculated oxygen isotope composition of the fluids.

Nine carbonate veins in samples obtained using standard ICDP protocols (denoted as samples) were first cleaned with 2-propanol and compressed air. Later, the surfaces of the veins were removed and discarded, followed by sampling the veins with a hand-held drill. Additionally, 12 samples of loose carbonate crystals from larger carbonate veins were hand-picked directly from the drilled cores, cleaned by ultrasonication in 100 ml dichloromethane (DCM) for 5 min at room temperature, and subsequently dried for 24 h at room temperature in a pre-combusted glass container covered with combusted aluminum foil. The carbonate vein samples were homogenized by hand using an agate mortar cleaned with DCM.

3.2. Powder X-Ray Diffraction

Crystallographic analyses were made using a Bruker AXS D8 Advance Powder X-ray Diffractometer (XRD) equipped with a Lynxeye superspeed detector (Bruker Corporation) with Cu Kα radiation, a voltage of 45 kV, and a current of 40 mA, with 2θ ranging between 10° and 60° with a step size of 0.01°, and measurement time of 1 s per step. The mineralogy was quantified using the program PowDll (Kourkoumelis, 2013) and the RRUFF database (Lafuente et al., 2015).

3.3. Optical Microscopy

Petrographic analyses were conducted using a polarizing microscope (Carl Zeiss Microscopy GmbH) and with cold cathode cathodoluminescence (CL) CL8200 Mk5-2 (Cambridge Image Technology Ltd). CL operating conditions were an accelerating voltage of 15 kV with a beam current of 250–300 µA.

3.4. Carbon Content and Isotopic Composition

Total and non-carbonate carbon contents and isotopic compositions were determined by combustion of 40–60 mg of a sample using a FlashEA 1112 Elemental Analyzer (EA) interfaced via a Conflo IV to a Delta V Plus Isotope Ratio Mass Spectrometer (MS) (all Thermo Fisher Scientific). The carbon content was calculated using two standards (Bodenstandards No. 5; 0.141%C, HEKAtech, and nicotinamide; 59.01%C, Thermo Fisher Scientific). Empty tin capsules were measured for blank correction. Analytical reproducibility of $\delta^{13}C_{TC}$ and $\delta^{13}C_{NCC}$ is ±0.11‰ (1σ). The detection limit for a reproducible carbon isotope measurement is about 10 µg C. Carbonate contents determined as total inorganic carbon (TIC) were calculated by the difference between TC and NCC.

$\delta^{13}C$ and $\delta^{18}O$ of TIC were measured on aliquots of whole-rock MBio samples, using a GasBench II connected to a Delta V mass spectrometer (both Thermo Fisher Scientific), as described in detail in Breitenbach and Bernasconi (2011). The average long-term reproducibility based on replicated standards is ±0.10‰ for $\delta^{13}C$ and 0.11‰ for $\delta^{18}O$ (1σ). The instrument is calibrated with the international standards NBS19 ($\delta^{13}C = 1.95$‰ and $\delta^{18}O = -2.2$‰) and NBS18 ($\delta^{13}C = -5.01$‰ and $\delta^{13}O = -23.01$‰). Samples as small as ~20 µg TIC can be analyzed with confidence and the precision mentioned above and are reported as replicates. We performed several test runs on cryptocrystalline magnesite collected at the Wadi Tayin Massif to guarantee a complete reaction of the carbonates in the bulk-rock samples.

A subset of carbonate veins was analyzed for clumped isotopes (Δ47) on a Kiel IV carbonate device interfaced with a ThermoFisher Scientific MAT253 isotope ratio mass spectrometer following the methodology described in detail in Meckler et al. (2014) and Müller, Violay, et al. (2017). Briefly, 100–110 µg of carbonate were reacted with three drops of 104% phosphoric acid (H_3PO_4) at 70°C. The evolved CO_2 was purified on a custom-built Porapak Q trap held at −40°C and measured on a MAT253 in micro-volume mode using the LIDI Protocol (Hu et al., 2014; Müller, Fernández, et al., 2017). The results are converted to the Carbon Dioxide Equilibrium Scale (CDES) using the carbonate standards ETH-1, ETH-2, and ETH-3 as described in Bernasconi et al. (2018). Dolomite values are reported for a reaction temperature of 70°C, the same temperature used to establish the calibration of Müller et al. (2019), and calcites are projected to 25°C. With 8–10 replicate analyses, the margins of error are ±3°C–5°C at the 95% confidence level (Fernández et al., 2017). $\delta^{13}C$ and $\delta^{18}O$ of TIC and $\delta^{13}C$ of TC and NCC are reported in conventional delta notation with respect to the Vienna Pee Dee Belemnite (VPDB) standard.

Clumped isotopes allow the calculation of the $\delta^{18}O$ of the fluid equilibrated with the carbonate vein. We used the calibration of Grossman and Ku (1986) for aragonite, O'Neil et al. (1969) corrected by Friedman and O'Neil (1977) for calcites, and Müller et al. (2019) for dolomites. The uncertainty for the calculated water $\delta^{18}O$

depends strongly on the number of possible replicate measurements, which control the uncertainty of the clumped isotope temperatures.

3.5. Radiocarbon Ages

Radiocarbon ages of decarbonated samples were measured by combustion with an Elemental Analyzer interfaced to a MICADAS Accelerator Mass Spectrometer (AMS) (Synal et al., 2007) equipped with gas-ion source at the Laboratory of Ion Bean Physics, ETH Zurich (Ruff et al., 2010; Wacker et al., 2010). Whole-rock TIC (MBio samples) and carbonate veins were measured by reaction with phosphoric acid reaction in vacutainers that were previously purged for 10 min with He, followed by direct injection of the produced CO_2 into the ion source of the AMS. The results are normalized against standard Oxalic Acid II (NIST SRM 4990C) and corrected with a radiocarbon blank CO_2 (IAEA C-1). In addition, IAEA-C2 and coral CSTD were measured in each run to test the accuracy of the measurement. The precision was better than ±5‰ on a modern standard. Radiocarbon data are expressed as $F^{14}C$ (fraction of modern carbon) and conventional ^{14}C ages, according to Reimer et al. (2004).

4. Results

One of the main differences between the two studied boreholes is the distinct amounts of dunite and carbonate veins (Figure 2). Hole BA1B drilled through 160 m of dunites at the top, followed by a 240 m thick harzburgite sequence. Hole BA3A drilled through 300 m of harzburgites without a major dunite sequence. The serpentinized dunites from Hole BA1B contain complex networks of distinct generations of aragonite, calcite, and dolomite veins in the uppermost 106 m, with an especially high concentration in the first 60 m of the core. In Hole BA3A, carbonate veins were found only in the uppermost ~5 m.

4.1. Carbonate Occurrences

Carbonates in the mantle rocks from the Wadi Tayin Massif occur as (a) veins, (b) as replacement of serpentine after pyroxene and olivine (Figure 3), and (c) as finely dispersed grains in the serpentinites. Carbonate veins were observed in both mafic and ultramafic rocks within the dunitic sequence of Hole BA1B, where they can make up to ~30 vol% of a rock sample in some shallow and oxidized rocks (Figure 3a). An example of the size of a sample from the rock cores is given in Figure 3b.

Carbonate veins are typically less than 1 cm wide, dissect grain boundaries, have kinked to irregular shapes, and show crosscutting or, more rarely, branching geometries. The veins are composed of aragonite, calcite, and dolomite in variable proportions and crosscut all other textures, indicating a late stage of formation (Figures 3b–3e). In some samples, at least two generations of carbonates coexist in the same rock (Figures 3c–3e). Dolomite veins are <2 mm wide and are found only in the top 25 and 5 m of the Holes BA1B and BA3A, respectively. Calcite veins are more common, are a few mm wide (Figures 3b–3g), and occur in the top 110 m at Hole BA1B. The most abundant and volumetrically dominant carbonate type are up to 1 cm wide aragonite veins in the top 33 m of Hole BA1B. Aragonite occurs in veins that crosscut the primary rock fabric (Figures 3c and 3d), postdate all secondary fabrics, and are the last carbonate vein to form.

Carbonates replacing serpentine mesh cores after pyroxene and olivine occur in the top 33 m of Hole BA1B; these are dominantly calcite and have an average grain size <20 μm (Figures 3f and 3g). Dispersed carbonates could not be identified microscopically but are indicated by whole-rock concentration and isotopic measurements and occur throughout the cores of both drill holes.

4.2. Carbon Isotopes

4.2.1. Bulk Rock Carbon in the Basement Rocks

The studied rocks show a wide range of total carbon contents, mainly reflecting varying carbonate abundance. Total carbon ranges from 215 ppm to 1.4 wt% with $\delta^{13}C_{TC}$ values from −15.9‰ to −5.8‰ (Table 1, Figures 4 and 5). Samples from Hole BA1B have slightly less TC than Hole BA3A, with an average concentration of ~786 ppm and higher concentrations observed in the upper 40 m. $\delta^{13}C_{TC}$ values of Hole BA1B range from −15.9‰ to −7.2‰. TC contents in serpentinites from Hole BA3A are homogenous and have an average value of ~1,065

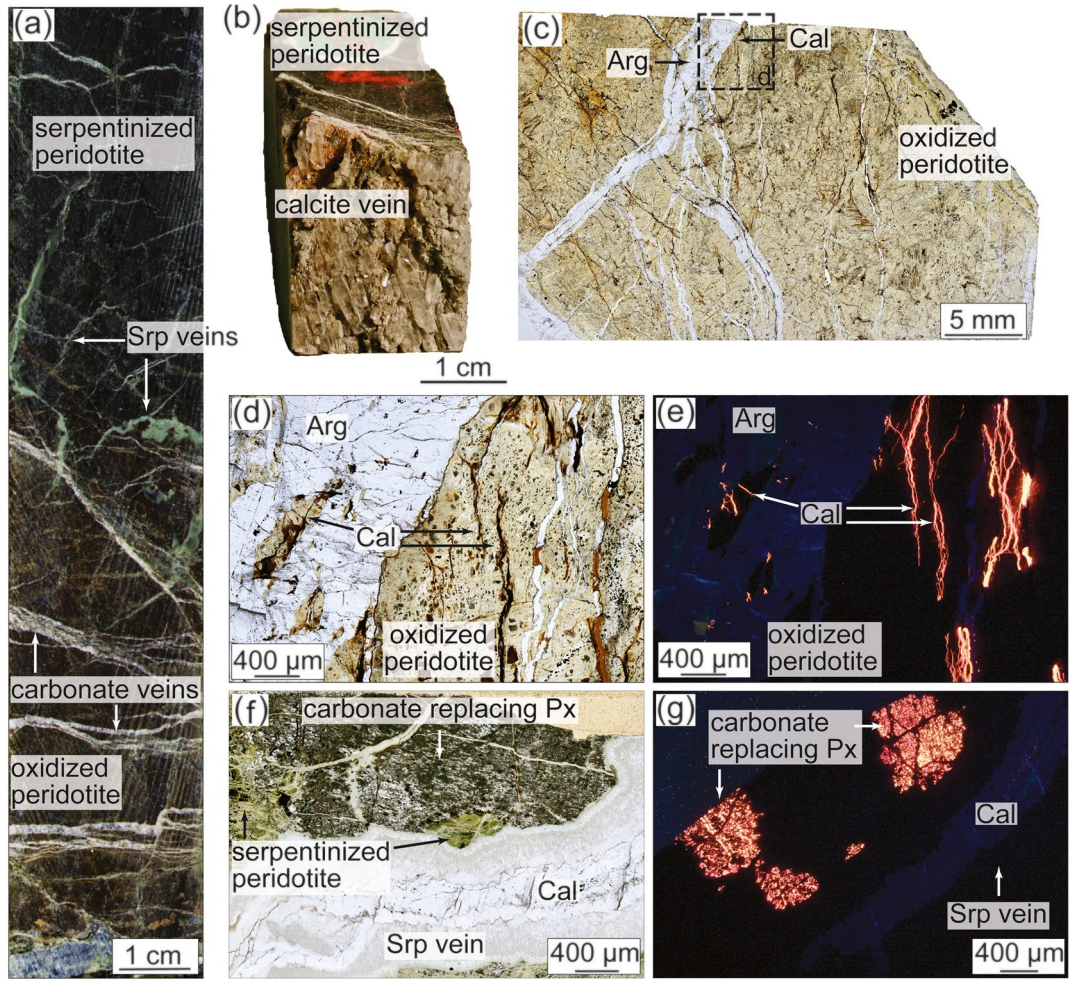

Figure 3. Core scans and photomicrographs of typical host lithologies and carbonates in the BA1B drillcore. (a) Example of a core of fully serpentinized dunite with multiple carbonate veins in a highly oxidized domain. The top of the core is less oxidized and contains fewer carbonate veins (sample BA1B_14M_3_68–82). (b) Large euhedral calcite crystals in a fracture of fully serpentinized dunite (BA1B_10Z_3_4–6). (c) Aragonite and Mg-rich calcite veins in serpentinized dunite. (d) Close-up of Figure 3c shows serpentinized dunite crosscut by aragonite veins, containing an earlier Mg-rich calcite vein generation (sample BA1B_4Z_4_12–17). (e) CL-image of the serpentinized dunite from Figure 3d showing non-luminescent aragonite and calcite with a strong orange luminescence. (f) Carbonates replace serpentine after pyroxene within a serpentinized peridotite and calcite reactivating serpentine vein (BA1B_17Z_1_17–22, PPL). (g) CL-image of carbonates replacing highly altered pyroxene within serpentinized peridotite and calcite reactivating serpentine vein. Arg, aragonite; Cal, calcite; Px, pyroxene; Srp, serpentine.

ppm, with one outlier with less than 700 ppm TC (~200 m). The $\delta^{13}C_{TC}$ values in Hole BA3A have a smaller range than in BA1B and lie between −9.5‰ and −5.8‰.

The serpentinized peridotites have wide TIC contents ranging from 57 ppm to 1.3 wt%, with $\delta^{13}C_{TIC}$ values from −15.0‰ to −4.7‰ (Figures 4b, 4c, 5b, and 5c). Most rocks from Hole BA1B have TIC contents around ~559 ppm, except for one sample from the uppermost oxidized core section with 1.3 wt%. The carbon isotope compositions of TIC in Hole BA1B range between −15.0‰ and −7.6‰, which is slightly more ^{13}C depleted than in BA3A. The dunite samples close to the dunite-harzburgite boundary show the most ^{13}C-depleted values with −13.4‰ within the dunitic sequence (Figure 4c). The harzburgites scatter around an average value of −10.9‰ and also show the most ^{13}C-depleted values close to the dunite-harzburgite boundary (Figure 4c). The harzburgites from Hole BA3A have homogenous TIC content ranging from 452 ppm to 0.1 wt%, with one outlier with less than 100 ppm (at ~200 m). The $\delta^{13}C_{TIC}$ values vary between −12.8‰ and −4.7‰ and generally decrease with increasing depth from 100 to 280 m (−11‰ to −4.7‰, Figure 5c).

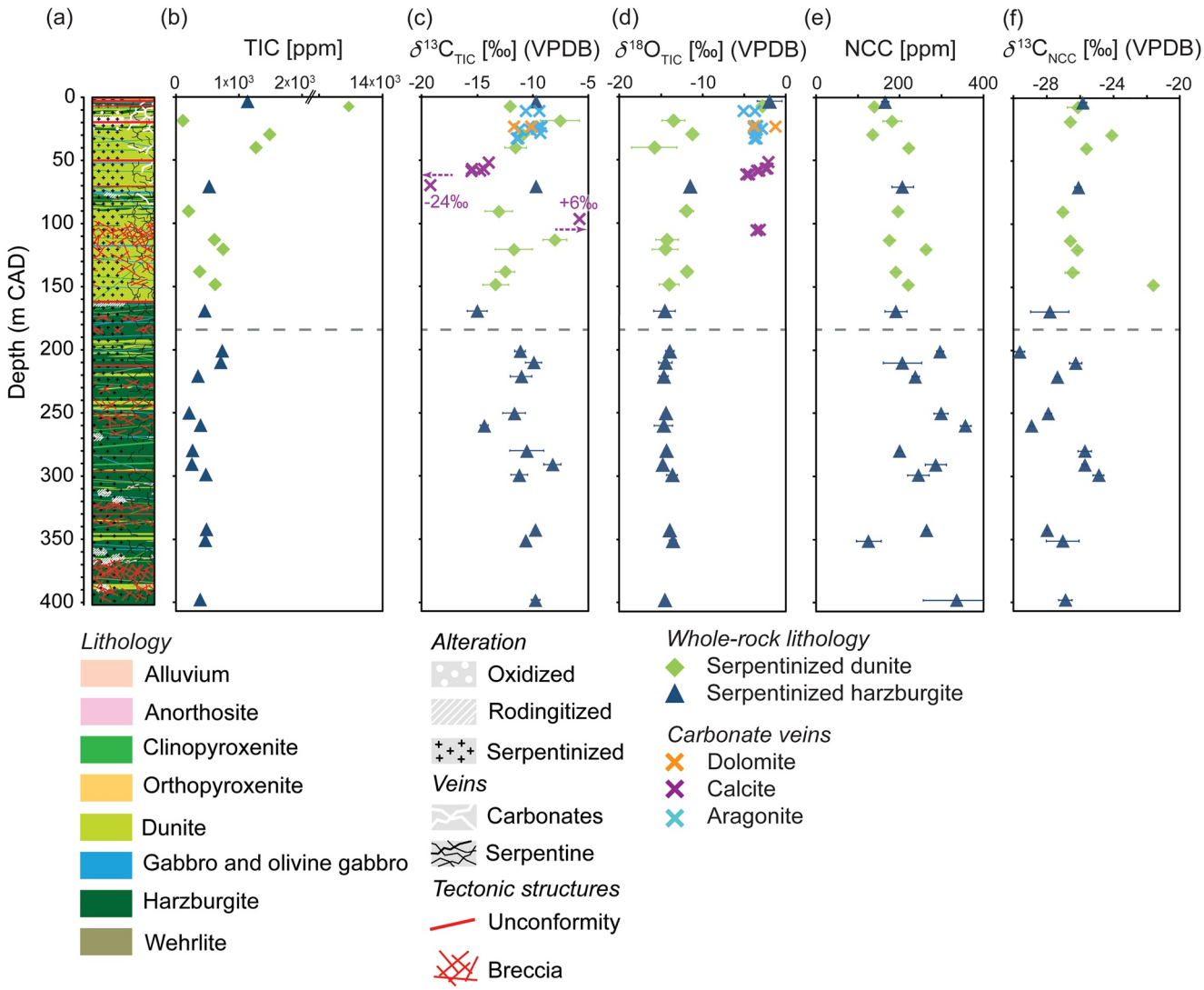

Figure 4. (a) Lithological profile of Hole BA1B, detailed information in Figure 2 (modified after Kelemen et al., 2020). Variations in (b) total inorganic carbon (TIC) content, (c) $\delta^{13}C_{TIC}$ values, (d) $\delta^{18}O_{TIC}$ values (e) total non-carbonate carbon (NCC) content, and (f) $\delta^{13}C_{NCC}$ values with Chikyu Adjusted Depth (CAD) from serpentinized dunite and harzburgite whole-rock MBio samples and carbonate veins from standard ICDP samples from the Wadi Tayin Massif. Carbon isotope composition of four calcite veins plot outside Figure 4c (denoted by arrows), two samples have more ^{13}C-depleted compositions, and two are more ^{13}C-enriched. Data are given in Table 2. The dashed line marks a brecciated zone close to the transition from dunite to harzburgite and separates whole-rock samples with distinct isotopic trends (see Section 5 for further details).

The non-carbonate carbon concentrations in both cores are low and range from 126 to 479 ppm, with $\delta^{13}C$ values ranging from −29.6‰ to −21.6‰, typical of organic carbon fractions measured previously in oceanic serpentinites (Delacour, Früh-Green, Bernasconi, Schaeffer & Kelley, 2008; Früh-Green et al., 2004; Schwarzenbach, Früh-Green, et al., 2013) (Figures 4e, 4f, 5e, and 5f). In Hole BA1B, NCC content is around ∼220 ppm and shows slightly more variation, higher concentrations, and overall lower $\delta^{13}C_{NCC}$ values in the harzburgite sequence in the lower part of the hole. $\delta^{13}C_{NCC}$ in Hole BA1B ranges from −29.6‰ to −24.1‰, with one outlier at −19.5‰ (Figure 4f). The serpentinized harzburgites from BA3A have the highest NCC concentrations and show an increase in NCC with depth in the first 100 m. Below this depth, the average NCC content is ∼190 ppm and is similar to concentrations in Hole BA1B. Three outliers show a higher content with values >400 ppm (Figure 5e). A difference in $\delta^{13}C_{NCC}$ is also seen between the top 100 m, with $\delta^{13}C$ of ∼−23.5 ‰, and the deeper section with $\delta^{13}C$ of ∼−26.3‰ (Figure 5f).

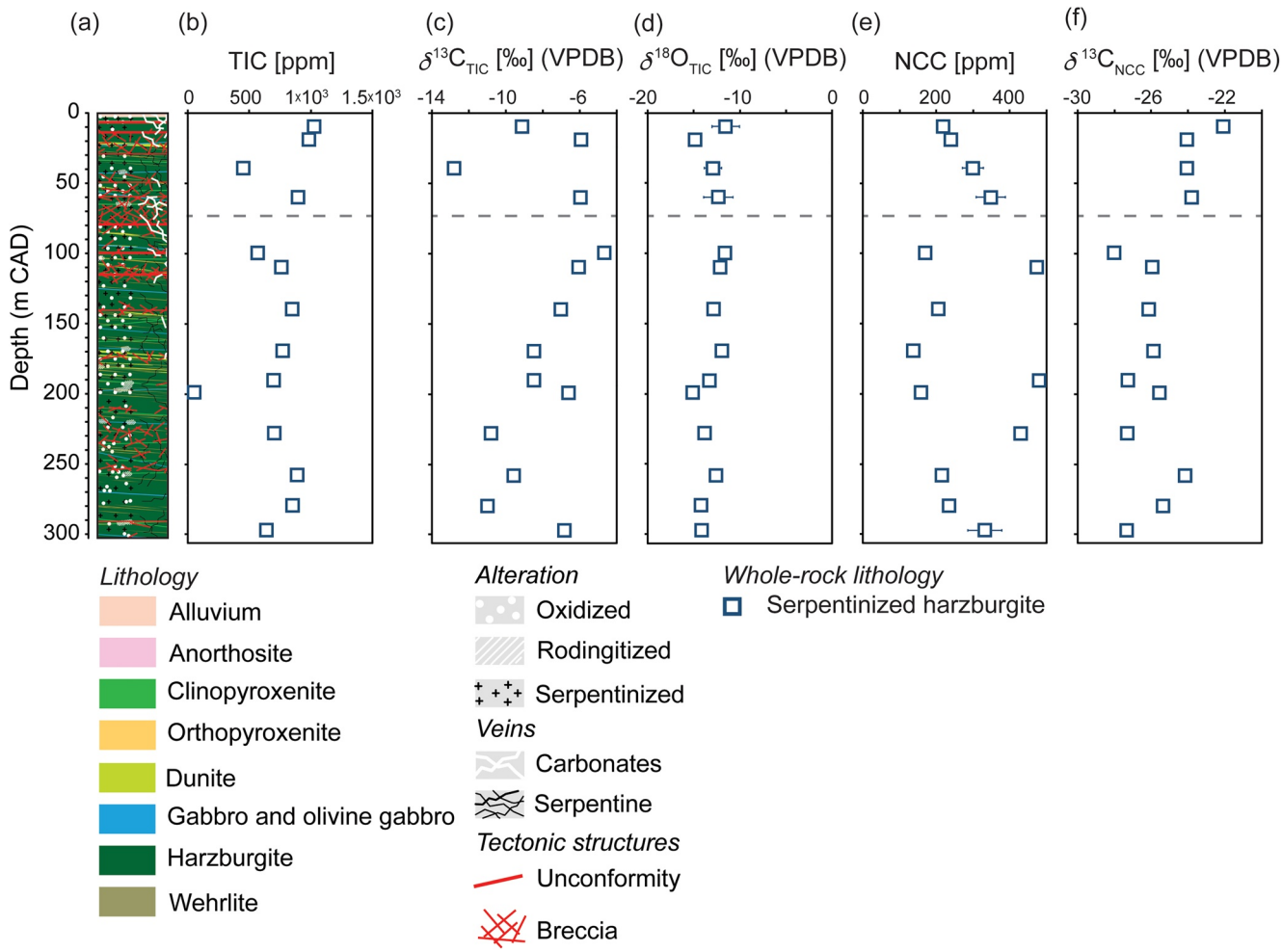

Figure 5. (a) Lithological profile of Hole BA3A, detailed information in Figure 2 (modified after Kelemen et al., 2020). Variations in (b) total inorganic carbon (TIC) content, (c) $\delta^{13}C_{TIC}$ values, (d) $\delta^{18}O_{TIC}$ values (e) total non-carbonate carbon (NCC) content, and (f) $\delta^{13}C_{NCC}$ values with Chikyu Adjusted Depth from serpentinized harzburgite whole-rock MBio samples from the Wadi Tayin Massif at the Samail Ophiolite. The dashed line marks a brecciated zone close to an unconformity that separates whole-rock samples with distinct isotopic trends (see Section 5 for further details).

4.2.2. Carbon Isotope Geochemistry of the Veins

Carbon isotope compositions of the veins are given in Table 2. Dolomite ($n = 2$) and aragonite ($n = 10$) were only found in the shallow part of Hole BA1B, and their $\delta^{13}C$ lie in a narrow range from −11.7‰ to −9.2‰. The calcite veins ($n = 9$) can be divided into three distinct groups with depth (Figure 4c). The deepest calcites at 105 m have ^{13}C-enriched compositions of ∼+5.7‰, calcites at 61 m have ^{13}C-depleted values of ∼−23.6‰, and the shallowest calcites at 56 m lie in a narrow range from −15.5‰ to −13.9‰.

4.3. Radiocarbon Dating

Five carbonate veins yielded ^{14}C ages ranging from 50,464 to 30,811 years, and the inorganic and non-carbonate carbon of six whole-rock MBio samples show ^{14}C ages from 29,750 to 293 years (Table 3, Figure 6). Because the veins often consist of multiple carbonate generations, ^{14}C values can represent a mixed-age rather than a single precipitation phase. The dolomite vein yield an age of 39,886 years, and calcites ages range from 42,386 to 30,811 years (Figure 6). The aragonite vein has the oldest ^{14}C age, with 50,464 years. The whole-rock samples yield much younger ages and show a distinct variation between the boreholes. In Hole BA1B, ^{14}C ages of TIC decrease from 29,750 years in the first 10 m to 293 years at ∼260 m depth, whereby the oldest age of whole-rock TIC (29,750 years) coincides with the latest carbonate vein with 30,811 years (Table 3). NCC in Hole BA1B

Table 3
Radiocarbon Ages of Carbonate Veins and Bulk-Rock MBio Samples From the Wadi Tayin Massif at the Samail Ophiolite

Site	Hole	Core	Section	Interval (cm) Top	Interval (cm) Bot.	Depth (m CAD) Top	Depth (m CAD) Bot.	Lithology	Mineralogy	Sample type	Carbon type	$F^{14}C$	$F^{14}C$ σ (%)	^{14}C ages (yrs)	^{14}C ages σ
BA	1B	3	2	73	85	7.34	7.46	Serpentinized dunite	–	Whole rock	Inorganic	0.025	0.001	29,750	321
BA	1B	3	2	73	85	7.34	7.46	Serpentinized dunite	–	Whole rock	Non-carbonate	0.185	0.002	13,574	101
BA	1B	8	4	34	35	23.28	23.29	Serpentinized dunite	Aragonite	Vein	Inorganic	0.002	25.104	50,464	2017
BA	1B	8	4	61	66	23.55	23.60	Serpentinized dunite	Dolomite	Vein	Inorganic	0.007	9.268	39,886	745
BA	1B	20	3	0	50	40.14	40.64	Serpentinized dunite	–	Whole rock	Inorganic	0.878	0.006	1,048	55
BA	1B	20	3	0	50	40.14	40.64	Serpentinized dunite	–	Whole rock	Non-carbonate	0.328	0.003	8,966	83
BA	1B	26	4	79	83	56.74	56.78	Serpentinized dunite	Calcite	Vein	Inorganic	0.009	6.899	37,464	554
BA	1B	28	2	68	72	61.29	61.33	Serpentinized dunite	Calcite	Vein	Inorganic	0.022	4.296	30,811	345
BA	1B	43	1	33	41	105.03	105.11	Olivine gabbro	Calcite	Vein	Inorganic	0.005	10.610	42,386	852
BA	1B	94	4	0	53	259.99	260.52	Serpentinized harzburgite	–	Whole rock	Inorganic	0.964	0.006	293	53
BA	1B	94	4	0	53	259.99	260.52	Serpentinized harzburgite	–	Whole rock	Non-carbonate	0.711	0.005	2,738	56
BA	3A	27	1	28	88	59.98	60.58	Serpentinized harzburgite	–	Whole rock	Inorganic	0.908	0.006	771	56
BA	3A	27	1	28	88	59.98	60.58	Serpentinized harzburgite	–	Whole rock	Non-carbonate	0.337	0.003	8,741	75
BA	3A	76	3	0	50	190.41	190.91	Serpentinized harzburgite	–	Whole rock	Inorganic	0.927	0.006	608	55
BA	3A	76	3	0	50	190.41	190.91	Serpentinized harzburgite	–	Whole rock	Non-carbonate	0.273	0.003	10,440	76
BA	3A	106	2	0	50	279.58	280.08	Serpentinized harzburgite	–	Whole rock	Inorganic	0.915	0.007	717	63
BA	3A	106	2	0	50	279.58	280.08	Serpentinized harzburgite	–	Whole rock	Non-carbonate	0.366	0.005	8,083	115

generally displays older ^{14}C ages than the TIC, except for a shallow sample in the first 10 m. Like TIC, ^{14}C ages of the NCC progressively decrease with increasing depth from 13,574 to 2,738 years (Table 3). The inorganic and non-carbonate carbon from Hole BA3A are more homogenous and yield ^{14}C ages of ~699 and ~9,088 years, respectively.

4.4. Oxygen Isotopes

The overall bulk-rock oxygen isotope composition of dispersed carbonate is relatively homogenous, with variations only seen in in the top 10 m of Hole BA1B, where two samples have a $\delta^{18}O_{TIC}$ of −2.8‰ and −2.0‰ (VPDB) (Figure 4d); below this depth in Hole BA1B $\delta^{18}O_{TIC}$ lies in a narrow range between −15.8‰ and −11.3‰. Variability is slightly higher in the serpentinized dunites. The $\delta^{18}O_{TIC}$ of the bulk rocks from Hole BA3A also lie in a narrow range from −15.1‰ to −11.5‰, similar to Hole BA1B (Figure 5d). Erosion and replacement of the first couple of meters with alluvium may have removed the shallow more ^{18}O-enriched carbonates at Hole BA3A. The $\delta^{18}O$ of the veins in Hole BA1B vary from −5.1‰ to −1.3‰ (Figures 4d and 6), similar to the $\delta^{18}O$ of the bulk samples of the first 10 m. Dolomites have $\delta^{18}O$ values from −3.9‰ to −1.3‰, calcites range from −4.8‰ to −2.2‰, and aragonites show uniform $\delta^{18}O$ values within a narrow range of −3.9‰ to −3.5‰, with one outlier at −5.1‰.

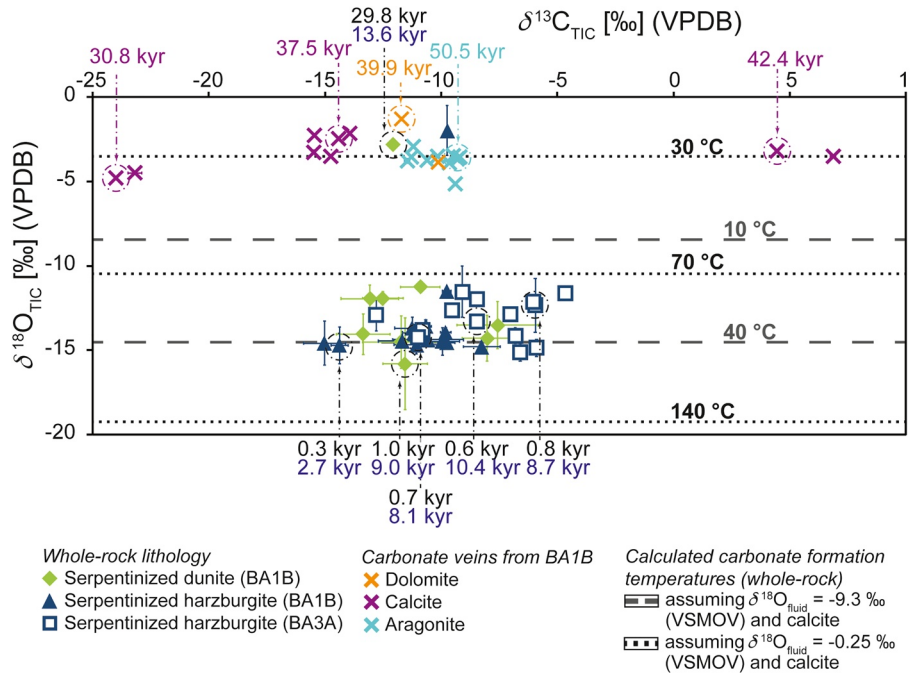

Figure 6. $\delta^{13}C_{TIC}$ versus $\delta^{18}O_{TIC}$ values of carbonate in serpentinized dunite and harzburgite from Hole BA1B and BA3A from the Wadi Tayin Massif of the Samail Ophiolite. Whole-rock MBio samples are compared with isotope values of calcite, aragonite, and dolomite veins from Hole BA1B. ^{14}C ages are given for five veins (color-coded according to carbonate phases) and six bulk rock samples distinguishing TIC (black numbers) and total NCC (blue numbers). Estimated temperatures are shown as dashed and dotted lines using average modern ground- and meteoric water $\delta^{18}O_{Fluid}$ of −0.25‰ and an average calculated $\delta^{18}O_{Fluid}$ of −9.3‰ (necessary for carbonate formation temperature of ~35°C for the dispersed carbonates).

4.5. Carbonate Precipitation Temperatures

4.5.1. Oxygen Isotope Thermometry of TIC in Whole Rock MBio Samples

Because of the low carbonate concentrations, it was not possible to measure clumped isotopes of the bulk dispersed carbonate. Carbonate formation temperatures were thus estimated from bulk oxygen isotope compositions using the oxygen isotope fractionation equation for calcite of O'Neil et al. (1969) corrected by Friedman and O'Neil (1977) and the equation of Müller et al. (2019) for dolomite. As radiocarbon dating indicates a recent formation age of these carbonates, to calculate $\delta^{18}O_{Fluid}$, we used the two endmembers of −3.0‰ and +2.5‰ (VSMOW) measured on modern groundwater and alkaline springs in the Samail Ophiolite as reported by Falk et al. (2016), Miller et al. (2016), and Nothaft, Templeton, Rhim, et al. (2021). Temperature estimates with $\delta^{18}O_{Fluid} = -3.0$‰ result in lower values. The calculated temperatures of formation range from 9 to 133°C, assuming that all carbonates are calcite, and from 30 to 204°C, assuming they are dolomite. The TIC concentration in whole-rock samples is below the detection limit of XRD, which limits the identification of the predominant carbonate phase. Due to the lack of dolomite and aragonite veins below 33 m and the measured Ca-OH-rich Type II fluid that was sampled in deeper parts of wells at the Samail Ophiolite (Kelemen et al., 2020), we assume that calcite is the main carbonate phase in the bulk rock samples.

The carbonates in the two shallow samples from Hole BA1B formed between 9 and 40°C (Table 1), which is consistent with the mean modern recharge temperature at shallow depth (<50 m) of ~32°C (Paukert Vankeuren et al., 2019). Dispersed carbonates below 10 m at Hole BA1B consistently have higher calculated temperatures between 57 and 133°C with no downhole trend. In Hole BA3A, dispersed carbonates exhibit a similar temperature range as in Hole BA1B with values from 59 to 127°C (Figure 6). These calculated formation temperatures are unrealistically high, considering the relatively young formation ages of less than 1,000 ^{14}C years and no modern heat source in the Samail Ophiolite. Therefore, we must assume that an ^{18}O-depleted fluid or disequilibrium processes rather than high formation temperatures cause the ^{18}O-depleted signatures of the dispersed carbonates. Assuming a mean modern recharge temperature of 35°C and using the oxygen isotope fractionation equation of

O'Neil et al. (1969) corrected with Friedman and O'Neil (1977), the estimated $\delta^{18}O_{Fluid}$ range from −11.5‰ to −7.0‰ (avg. −9.3‰, Figure 6).

4.5.2. Clumped Isotope Temperatures of Carbonate Veins

Clumped isotope temperatures vary from 26 to 43°C (Table 2), which are in the range of the ^{18}O-based temperatures of shallow bulk rocks of Hole BA1B. Dolomites have clumped isotope temperatures of $T_{\Delta47}$ = 29–43°C. The calcites show $T_{\Delta47}$ of 28–39°C, and the aragonite veins yield $T_{\Delta47}$ of 26–39°C. Calculated oxygen isotope values of the fluid in equilibrium with the carbonates are ∼0‰ ± 2‰. Fluids in equilibrium with dolomite veins have a restricted range of −1.3‰ to −1.0‰, whereas fluids forming the calcite veins have more variable values from −1.7‰ to +1.3‰, with no distinction between different depths. Similarly, the $\delta^{18}O$ of the fluids that precipitated aragonites lie in a range of −1.8‰ to +0.6‰.

5. Discussion

Our observations and data suggest that the studied rocks in the Wadi Tayin Massif were affected by two distinct phases of carbonate formation during the last 50 kyr (or longer). (a) The carbonate veins formed during focused fluid flow, at temperatures between 26°C and 43°C, from 30 kyr to over 50 kyr before present, and are limited to the dunitic sequence of BA1B and shallow parts of BA3A and with variable DIC sources. (b) Pervasive disperse carbonates precipitated from an ^{18}O-depleted fluid at moderate temperatures, with a ^{13}C-depleted carbon source, likely derived from the respiration of organic matter (OM). Scicchitano et al. (2020) reported different stages of serpentinization and provided evidence for early seafloor hydration and alteration from samples of Hole BA1B. Similarly, Noël et al. (2018) suggest seawater derived-fluids leading to the earliest carbonate formation in samples from Wadi Dima, Wadi Tayin Massif, north-west of the OmanDP Site and de Obeso and Kelemen (2018) suggest seawater derived-fluids leading to serpentinization and carbonization of peridotites from Wadi Fins, south-east of the OmanDP Site BA. However, our study found no evidence for carbonate formation during the oceanic phase of serpentinization of the Samail Ophiolite. In the following, we discuss the evolution of carbonate formation in the Wadi Tayin Massif and the implications for organic carbon storage in ultramafic rocks.

5.1. Carbonate Vein Precipitation and Focused Fluid Flow

Macroscopic brecciation and veining of the peridotite indicate that hydration and carbonization were facilitated by deformation. The infiltration of fluids was likely controlled by continuous fracture planes and micro-fracturing caused by serpentinization, forming permeability pathways and channeling the fluids along specific domains of the mesh-textured peridotite. We argue that focused fluid flow leads to the formation of carbonate veins in the more permeable dunitic sequence of Site BA, especially within the first meters, with $T_{\Delta47}$ indicating precipitation temperatures of 26–43°C (Table 2) and radiocarbon ages from 30 kyr to >50 kyr (Table 3).

The clumped isotope temperatures of the veins from Hole BA1B are in the same range as those previously reported for young carbonates (clumped isotope temperatures between 23°C and 43°C) that formed during present-day weathering in the Samail Ophiolite (Streit et al., 2012). In addition, our data complement earlier thermometry estimates in the ophiolite that indicated slightly higher oxygen isotope-based temperatures of 20–60°C for calcite veins in peridotite from outcrops and roadcuts with ^{14}C ages from 8 kyr to >50 kyr (Kelemen et al., 2011; Mervine et al., 2014) and clumped and oxygen isotope temperatures between ambient and 60°C for modern to >45 kyr old travertine (Clark et al., 1992; Falk et al., 2016; Kelemen et al., 2011; Mervine et al., 2014). Furthermore, our data correspond to seawater-derived carbonates from Wadi Fins formed at temperatures from $T_{\Delta47}$ = 22–46°C during the Cretaceous and Paleogene; however, carbonates from Wadi Fins are related to different processes (de Obeso & Kelemen, 2018).

The calculated formation temperatures from carbonate veins in our study are similar to those reported in the literature; however, the ages of the drillcore carbonate veins suggest a shorter period of formation. We propose that low-temperature alteration by focused fluid flow was predominant in the shallow dunitic sequence and changed over time to pervasive alteration without the formation of carbonate veins below the present-day surface. However, as previously observed by Noël et al. (2018), carbonate veins can represent multiple phases of formation, and the ^{14}C values could represent a mixture of radiocarbon dead (>50 kyr) and modern carbonate. Thus, the observed formation ages are consistent with previous radiocarbon ages of carbonates within peridotites of the

Samail Ophiolite. Carbonates from listvenite and the metamorphic sole formed during the Cretaceous at much higher temperatures (clumped isotope temperatures between 52°C and 247°C, Beinlich, Plümper, et al., 2020; Falk & Kelemen, 2015) and, similar to those of the Wadi Fins, are related to different processes.

The carbon isotope ratios of the carbonate veins from Hole BA1B (δ^{13}C of −24.0‰ to +6.9‰) indicate ^{13}C-depleted carbon as a predominant carbon source except for the two calcite veins characterized by positive ^{13}C values (Figure 6). A range of δ^{13}C from −15‰ to −8‰ in carbonates in Oman has previously been attributed to the respiration of organic matter in soils (Clark et al., 1992) and is consistent with values from dolomite, aragonite, and most of the calcite veins in our study. In addition, the carbon isotope compositions of the veins are in the same range as those of the DIC in Type I fluids (Mg^{2+} - HCO_3^-) in several wells in the Wadi Tayin Massif (−13.9‰ to −10.9‰, Nothaft, Templeton, Rhim, et al., 2021). Thus, we argue that ^{13}C-depleted carbon from organic matter respiration, mixed with atmospheric CO_2 (δ^{13}C = ∼−7‰, Clark et al., 1992), and possibly bicarbonate from the dissolution of limestones represent the main carbon sources for the carbonate veins.

Biologically mediated respiration of OM can occur *ex situ*, and ^{13}C-depleted carbon can be transported via the percolating fluid to the system and *in situ* by organisms inhabiting the ultramafic rocks. Recent microbiological and metagenomic studies showed that microbial life can be sustained within the lithosphere and that microbial utilization of H_2, CH_4, and formate may be common in different serpentinization systems (Brazelton et al., 2012; Curtis et al., 2013; Daae et al., 2013; Etiope & Sherwood Lollar, 2013; Lang et al., 2018; Ohara et al., 2012; Schrenk et al., 2013). Furthermore, recent studies on drillcores from Site BA1B and BA3A showed cell counts ranging from as high as 10^7 cells g^{-1} in heavily veined areas down to 10^1 cells g^{-1} in the interior of some peridotites (Templeton et al., 2021). These cell counts are comparable and, in part, higher than previously reported from other areas such as the Atlantis Massif (10^1–10^3 cells g^{-1}, Früh-Green et al., 2018; Orcutt et al., 2017), the Atlantis Bank at the Southwest Indian Ridge (10^2–10^3, Li et al., 2020), and the deep continental basalts in the Decca traps (10^5 cells g^{-1}; Dutta et al., 2018).

Two calcite veins at about ∼61 m depth have more ^{13}C- depleted values (δ^{13}C = ∼−24‰, Figures 4c and 6) than most of the other veins. This may indicate a stronger influence of Type II fluids (Ca^{2+}-OH^-) with a reported DIC value of −30‰ (NSHQ04, Nothaft, Templeton, Rhim, et al., 2021) or input of ^{13}C-depleted inorganic carbon from anaerobic oxidation of methane. Nothaft, Templeton, Rhim, et al. (2021) reported 16S rRNA data that showed the presence of microbes capable of CH_4 oxidation, which produces highly ^{13}C-depleted inorganic carbon (Drake et al., 2015; Pedersen et al., 1997). Alternatively, the more ^{13}C-depleted carbonate veins could also be explained by a Rayleigh distillation of the DIC in the fluid caused by progressive carbonate precipitation. After removal of about 90% DIC with a δ^{13}C of −20‰ by carbonate precipitation with a fractionation factor between DIC and calcite of 2‰ (i.e., with the calcite being 2‰ heavier than the DIC), the residual DIC in solution reaches δ^{13}C of ∼−25‰. This residual DIC could result in precipitation of carbonates with δ^{13}C = ∼−23‰, leading to the range we measure in the carbonate veins.

A further endmember is indicated by two calcite veins at ∼105 m depth, which are characterized by more ^{13}C-enriched values potentially related to methanogenic activity (Figures 4c and 6). Methanogenic archaea reduce CO_2 to methane leading to a strong isotopic enrichment of the residual DIC (Deppenmeier et al., 1996) by the preferred removal of ^{12}C. Recent sequencing studies showed a widespread presence of the 16S rRNA gene affiliated with methanogens in well waters close to Site BA (Nothaft, Templeton, Rhim, et al., 2021). However, both veins that show δ^{13}C of +6‰ are located below 100 m (BA1B), which, combined with highly alkaline conditions, may limit the ability of micro-organisms to thrive but does not exclude it. We propose that most of the ^{13}C-enriched DIC is transported with the percolating fluid and *in situ* production only contributes to a minor amount.

Assuming that the carbonates were precipitated in isotopic equilibrium, we can calculate the δ^{18}O of the fluid using clumped isotope temperatures. The calculated $\delta^{18}O_{Fluid}$ lie in a range from −2‰ to +1.3‰ ± 2‰, overlapping with the values of −3.0‰ to +1.9‰ from the modern ground- and well-waters (Miller et al., 2016; Nothaft, Templeton, Rhim, et al., 2021; Paukert Vankeuren et al., 2019). We propose that late post-obduction serpentinization leads to the formation of low-temperature carbonates caused by a fracture-controlled fluid circulation comparable to modern groundwater of Type I and Type II. Additionally, the carbonate mineralogy shows a distinction between shallow areas (top 33 m) with dolomite and aragonite and deeper areas (52–106 m) with calcite only, which is consistent with a change from an Mg^{2+}-rich Type I to a Ca^{2+}-rich and Mg^{2+}-poor Type II fluid at ∼50 m below the surface. Previous studies have proposed that Type I fluids mixed with DIC lead to the

formation of magnesite and dolomite and Type II fluids exposed to the atmosphere to the precipitation of calcite (Barnes et al., 1978, 1967; Barnes & O'Neil, 1969; Bruni et al., 2002; Cipolli et al., 2004; Kelemen et al., 2011; Neal & Stanger, 1985; Paukert et al., 2012).

The precipitation of low-temperature dolomite is still poorly understood. Previous studies showed that abiotic formation of dolomite at low temperatures is inhibited by slow reaction kinetics (Sibley et al., 1987) caused by a lack of nucleation sites (Bosak & Newman, 2003), cation desolvation (Brady et al., 1996), sulfate inhibition (Baker & Kastner, 1981), and lack of solution supersaturation (Arvidson & Mackenzie, 1999). Microbial activity, however, has been shown to catalyze dolomite formation by sulfate reduction, methanogenesis, methanotrophy, sulfide oxidation, and aerobic respiration (Kenward et al., 2009; Moore et al., 2004; Moreira et al., 2004; Sánchez-Román et al., 2009; Vasconcelos et al., 1995). Newman et al. (2020) and Nothaft, Templeton, Rhim, et al. (2021) reported rRNA gene sequences and lipid biomarkers that suggest that sulfate-reducing bacteria, methanogens, and methanotrophs are widespread in the aquifer at the Wadi Tayin Massif. Consequently, microbial-mediated dolomite formation would be possible within serpentinized peridotites from Site BA. However, we suggest that a high Mg/Ca ratio of a Type I groundwater (ranging between 7 and 66, Nothaft, Templeton, Rhim, et al., 2021) is probably the dominant controlling factor, and microbial activity only contributes to a minor amount. More analyses of the influence of microbial activity in forming Mg-rich carbonate in these rocks are necessary to evaluate the potential effect of microbial metabolism on dolomite precipitation in ultramafic rocks.

The comparison of $\delta^{13}C$ values of carbonate veins of our study ($\delta^{13}C = -24.0‰$ to $+6.9‰$) with literature data shows that only some of the carbonates coincide with reported values for outcrops of the Samail Ophiolite (Figure 7a). In the uppermost 33 m, aragonite and dolomite veins lie in a similar but slightly more ^{13}C-depleted range. Deeper calcite veins only overlap with a single measurement from Noël et al. (2018). The comparison with literature data from different ophiolites worldwide (Figure 7b) shows a similar pattern, whereby the carbonate veins from the top 60 m of Hole BA1B coincide with previously reported values, including the shallower calcite veins. The higher variability in $\delta^{18}O$ reflects the variability of the oxygen isotope composition of meteoric waters with latitude, distance from the vapor source, and amount of rainout (Rozanski et al., 1993), which explains the more enriched values at Oman. We argue that the deeper calcite veins (depth >60 m) are caused by deeper groundwater circulation and have not been reported earlier for Oman because drillcores were not available and previous studies focused on analyses of samples from outcrops.

5.2. Recent Dispersed Carbonate Precipitation

The influx of groundwater during later alteration of the peridotites occurs via a fine network along grain boundaries and micro-fractures, which leads to the formation of dispersed carbonates with progressive hydration of the entire Wadi Tayin Massif. Dispersed carbonates are the predominant carbonate occurrence and are not limited to specific lithology, depth, or cores, which suggest that pervasive fluid flow and alteration is the predominant carbonization mechanism at the Wadi Tayin Massif. ^{14}C ages between 1050 and 290 years indicate that dispersed carbonate precipitation is recent and thus that hydration and carbonization of the ultramafic rocks is an ongoing process. This is consistent with the presence of highly alkaline spring- and well-waters, which demonstrate ongoing serpentinization in the Samail Ophiolite today (Kelemen et al., 2011; Kelemen & Matter, 2008; Neal & Stanger, 1985).

The dispersed carbonates have, similar to the carbonate veins, an isotope signature indicating a ^{13}C-depleted DIC source ($\delta^{13}C$ from $-15.0‰$ to $-4.7‰$, Figure 6) from biologically mediated respiration of OM mixed with atmospheric CO_2 (see Section 5.1 for more details). The dispersed carbonates are characterized by variable $\delta^{13}C$ that show no correlation with TIC content, ^{14}C ages, and/or oxygen isotope composition. However, they show distinct isotopic compositions in both sites above and below a highly brecciated zone at ~180 m in Hole BA1B and above and below an unconformity associated with a highly brecciated zone at ~70 m in Hole BA3A (Figures 4c and 5c). Katayama et al. (2020) showed that dunites from Hole BA1B have a higher permeability than the harzburgites, leading to higher and focused fluid flux within the dunites and channeling of fluids with different compositions depending on the location within the borehole. We propose that the observed changes in the carbon isotope composition reflect changes in the hydrology of the system and that the percolating fluid at the Wadi Tayin Massif is heterogeneous with variable contributions of biologically derived carbon. Thus, fluid mixing is likely a common process at the Wadi Tayin Massif, and fluids can infiltrate the basement at different times and

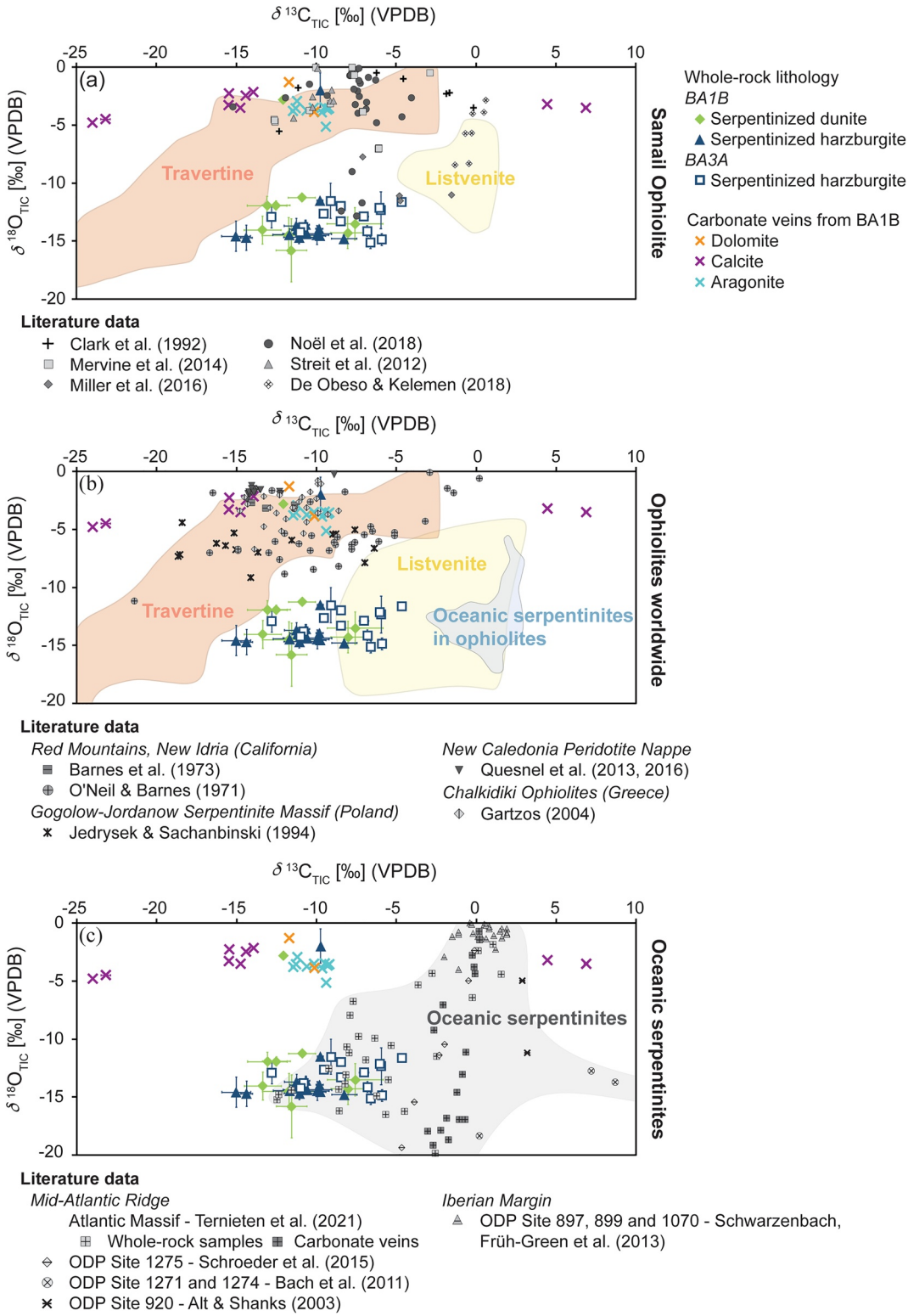
δ 13C_TIC [‰] (VPDB)
δ 18O_TIC [‰] (VPDB)
(a)
Travertine
Listvenite
Samail Ophiolite
Whole-rock lithology
BA1B
Serpentinized dunite
Serpentinized harzburgite
BA3A
Serpentinized harzburgite
Carbonate veins from BA1B
Dolomite
Calcite
Aragonite
Literature data
Clark et al. (1992)
Mervine et al. (2014)
Miller et al. (2016)
Noël et al. (2018)
Streit et al. (2012)
De Obeso & Kelemen (2018)
(b)
Travertine
Listvenite
Oceanic serpentinites in ophiolites
Ophiolites worldwide
Literature data
Red Mountains, New Idria (California)
Barnes et al. (1973)
O'Neil & Barnes (1971)
Gogolow-Jordanow Serpentinite Massif (Poland)
Jedrysek & Sachanbinski (1994)
New Caledonia Peridotite Nappe
Quesnel et al. (2013, 2016)
Chalkidiki Ophiolites (Greece)
Gartzos (2004)
(c)
Oceanic serpentinites
Oceanic serpentinites
Literature data
Mid-Atlantic Ridge
Atlantic Massif - Ternieten et al. (2021)
Whole-rock samples
Carbonate veins
ODP Site 1275 - Schroeder et al. (2015)
ODP Site 1271 and 1274 - Bach et al. (2011)
ODP Site 920 - Alt & Shanks (2003)
Iberian Margin
ODP Site 897, 899 and 1070 - Schwarzenbach, Früh-Green et al. (2013)

Figure 7.

structural levels such as fracture planes, micro-fractures, and grain boundaries, causing highly heterogenous signatures controlled by tectonic features.

When assuming a modern groundwater oxygen isotope composition, calculated oxygen isotope temperatures of the dispersed carbonates range from 57 to 133°C. These temperatures are unrealistically high, considering the relatively young formation ages, shallow depths, and lack of apparent heat source. Paukert Vankeuren et al. (2019) estimated a mean modern recharge temperature of 32°C at depths <50 m in the peridotite aquifers of Oman. The highly ^{18}O-depleted compositions in carbonates can either be caused by (a) isotopic disequilibrium precipitation during rapid carbonate formation in high pH fluids or by (b) precipitation from a much more ^{18}O-depleted fluid than present-day groundwater.

1. Clark and Fontes (1990) described a substantial depletion in ^{13}C and ^{18}O of travertines in the Samail Ophiolite during precipitation of carbonates caused by CO_2 uptake from the atmosphere and carbonate precipitation at the air-fluid interface under high pH conditions. A strong kinetic isotope fractionation on the order of 19‰–24‰ at 25°C occurs by the unidirectional reaction of $CO_{2(aq)}$ with OH^- molecules, which are more ^{18}O-depleted than H_2O molecules (Zeebe, 2020), leading to strongly ^{18}O and ^{13}C depleted carbonates. Previous studies from Miura et al. (2011) provided evidence for H_2O and CO_2-rich inclusions within olivine and orthopyroxene in harzburgites from the northern Samail Ophiolite. The aqueous fluid reacts with the surrounding mineral and produces alkaline, H_2, and CH_4-containing fluid inclusions. In addition, Nothaft, Templeton, Rhim, et al. (2021) concluded that fluid inclusions are necessary to explain the isotopic signature of CH_4 in the well waters of Site BA. If our samples contained a higher amount of alkaline fluid inclusions, OH^- within the inclusion might become exposed to the atmosphere while crushing the rock as part of the sample preparation and reacting with CO_2. This reaction could lead to dispersed carbonate precipitation with a highly depleted δ^{18}O composition. Thus, the ^{14}C ages (1,050–290 years) could represent a mixture of predominantly modern precipitated contamination and only a minor contribution of older carbonates formed during hydration of the Wadi Tayin Massif.
   However, the carbon isotope signature is not as negative as commonly observed in carbonates precipitated from high pH fluids (Travertine range in Figures 7a and 7b, Clark et al., 1992; Falk et al., 2016; Mervine et al., 2014). Furthermore, petrographic observation of serpentinized peridotites from Site BA do not show noticeable high concentrations of fluid inclusions. In addition, previous analyses performed in our laboratory on MBio-type samples recovered from the Atlantis Massif, Mid-Atlantic Ridge, addressing similar questions, have not found conspicuous ^{18}O-depleted carbonates (Ternieten et al., 2021). Therefore, we conclude that contamination of carbonates during sample preparation is unlikely to explain the highly depleted ^{18}O carbonates or only contribute a negligible influence on the isotopic signal.
2. Another explanation is that the dispersed carbonates formed from a much more ^{18}O depleted fluid than present-day groundwater. Assuming calcite as the dominant carbonate phase and a mean formation temperature of 35°C, the δ^{18}O of the percolating fluid would be between −11.5‰ and −9.3‰. Scicchitano et al. (2020) reported *in situ* oxygen isotope analysis of serpentine minerals from Hole BA1B and proposed three serpentinization stages with fluids with distinct ^{18}O values. Their Stage II serpentinization by meteoric water, which formed late banded chrysotile veins, required a fluid with a δ^{18}O of ∼−7‰, much lower than modern groundwater. Other evidence of meteoric waters with more depleted δ^{18}O values are from speleothem fluid inclusions from the last interglacial period (∼125kyr), from a cave in northern Oman with δ^{18}O values of ∼−7.8‰ (Fleitmann et al., 2011; Nicholson et al., 2020). In addition, Streit et al. (2012) reported calculated δ^{18}O of the

Figure 7. Whole-rock $\delta^{13}C_{TIC}$ values versus $\delta^{18}O_{TIC}$ of serpentinized peridotites from Hole BA1B and BA3A, and calcite, aragonite, and dolomite veins from Hole BA1B from the Wadi Tayin Massif. Carbonates of this study are compared to samples from (a) the Samail Ophiolite, (b) ophiolites worldwide, and (c) oceanic serpentinites. (a) The range from listvenites (Beinlich, Plümper, et al., 2020; Falk & Kelemen, 2015) and travertine/carbonate crusts from alkaline springs (Clark et al., 1992; Falk et al., 2016; Mervine et al., 2014) are marked as yellow and orange fields, respectively, and compared to other literature data of carbonate veins within serpentinized peridotites. (b) The range from listvenites is indicated by a yellow field and is defined by values from (a) and additional from the Appalachians and Advocate Listvenite in Canada (Auclair et al., 1993; Menzel et al., 2018), Linnajavri and Leka Ophiolite in Norway (Beinlich et al., 2012; Bjerga et al., 2015), and the Birjand Ophiolite in Iran (Boskabadi et al., 2020). The range for oceanic serpentinites is defined by values from the Northern Apennine ophiolites in Italy (Schwarzenbach, Früh-Green, et al., 2013) and for travertine deposits by values from (a), the Voltri Massif and different deposits in California (O'Neil & Barnes, 1971; Schwarzenbach, Lang, et al., 2013), indicated by blue and orange fields, respectively. Values from carbonate veins from the Red Mountains and New Idria in California, Gogolow-Jordanow serpentinite massif in Poland, from the New Caledonia peridotite nappe in New Caledonia, and various ophiolites located in Greece. (c) Isotopic composition of subseafloor ultramafic hosted hydrothermal carbonates and inorganic carbon from oceanic serpentinites, and gabbro-intruded ultramafic rocks from the Iberian Margin and the Atlantis Massif are shown (Alt & Shanks, 2003; Bach et al., 2011; Barnes et al., 1973; Gartzos, 2004; Jedrysek and Sachanbinski, 1994; Quesnel et al., 2013, 2016; Schroeder et al., 2015).

fluid in equilibrium with magnesite veins of −7.7‰. These previous studies suggest that ^{18}O-depleted fossil groundwaters are possible within the Samail Ophiolite and that the dispersed carbonates may have precipitated from a fluid that has led to late-stage serpentinization.

5.2.1. Dispersed Carbonates as Products of Deeper Fluid Circulation?

The carbon and oxygen isotope signatures of the dispersed carbonates are distinct from carbonate veins from our study and other localities in the Samail Ophiolite. Previous studies include carbonate veins in peridotites formed during present-day weathering (Mervine et al., 2014; Streit et al., 2012) from outcrop and drilled samples of listvenite and the metamorphic sole (Beinlich, Plümper, et al., 2020; Falk & Kelemen, 2015), travertines (Clark & Fontes, 1990; Falk et al., 2016, and reference therein), and Cretaceous carbonates (de Obeso & Kelemen, 2018, Figure 7a). However, the dispersed carbonates in our study show similar compositions to the early dolomite veins from Noël et al. (2018) and matrix carbonates from drill cuttings of the wells NSHQ04 and NSHQ14 at Site BA (Miller et al., 2016, Figure 7a). The dolomite veins have been attributed to pervasive fluid flow at high-temperature conditions at the seafloor in the Jurassic (Noël et al., 2018). However, the radiocarbon ages of our samples exclude such an early formation for the dispersed carbonate at Site BA. The same observation is made by comparing the dispersed carbonates with carbonates from other ophiolites (Figure 7b). The dispersed carbonates have distinct isotopic compositions that distinguish them from previously analyzed carbonates, except Newfoundland listvenites (Auclair et al., 1993), although their formation is related to different chemical processes than the dispersed carbonates of this study. The isotopic compositions of the dispersed carbonates overlap with those formed during ocean-floor serpentinization at the Atlantis Massif (Figure 7c, $\delta^{13}C_{TIC} = -14‰$ to $-2‰$; $\delta^{18}O_{TIC} = -17‰$ to $-6‰$; Ternieten et al., 2021). However, the ^{14}C ages exclude an early ocean-floor serpentinization-related origin of the dispersed carbonates. These results provide evidence that radiocarbon analyses are essential for a correct interpretation of the origin of carbonates.

Our study suggests that dispersed carbonates precipitated by mixing modern ^{13}C-depleted meteoric water with deeper fossil carbon-depleted groundwater with a ^{18}O-depleted composition. They occur throughout the Wadi Tayin Massif, indicating large-scale hydration and representing the most recent carbonate formation, whereas older generations may have been dissolved. Serpentinized peridotites in outcrops often contain abundant carbonate veins, which may overprint the lower amounts of dispersed carbonates. This could explain the low number of previously reported low-temperature carbonates with ^{18}O-depleted signatures in other studies of the Samail Ophiolite. We suggest that micro-fracturing caused by serpentinization provides the percolating fluid pathway and that they probably became one of the main natural hydraulic plumbing systems contributing to modern wadis and alkaline springs in the Samail Ophiolite. The occurrence of relatively young carbonates provides further evidence for the ongoing weathering and active serpentinization in the mantle section of the Samail Ophiolite. However, further investigations of carbonate formation are necessary to understand the evolution from initial to recent carbonization.

5.3. Serpentinites as a Microbial Habitat and Sink for Organic Carbon?

Recent studies have shown that the ultramafic basement can sustain microbial life (Barry et al., 2019; Colman et al., 2017; Fullerton et al., 2019). Furthermore, the isotopic composition of carbonates in our study shows that ^{13}C-depleted carbon, predominantly from biological mediation respiration of OM, is a significant component in the system. Serpentinites from the wells NSHQ14 and NSHQ04 have very variable TOC concentrations of <0.01–0.37 wt% (Miller et al., 2016), whereby the highest values may be overestimated due to residual magnesite in the samples.

The highest NCC content measured in our study is ~500 ppm, and both boreholes show distinct trends that can be correlated to unconformities, fractures, and heavily brecciated zones. Hole BA1B shows a shift to slightly higher NCC concentrations and lower $\delta^{13}C_{NCC}$ at the transition from dunites to harzburgites (Figures 4e and 4f), potentially indicating a higher input from microbial activity. However, Hole BA3A shows a change to more ^{13}C-depleted values below the unconformity at ~80 m (Figure 5e), but only locally higher concentrations of total NCC content. We propose that the observed changes in the carbon isotope composition of NCC reflect changes in the hydrology of the system and that a higher fluid flow in more permeable zones leads to the removal of previously present NCC by oxidation. This explains the lower NCC content in the uppermost highly oxidized 10 m of BA3A and dunitic sequence at Hole BA1B, which are influenced by Mg-HCO_3^--rich Type I fluids (Barnes

& O'Neil, 1969). Previous studies of nearby wells WAB 104, WAB 105, and BA1A showed that anoxic Type I fluids contain oxidants such as nitrate that allow oxidation of the NCC (Nothaft, Templeton, Boyd, et al., 2021; Nothaft, Templeton, Rhim, et al., 2021).

Higher fluid flow is, in general, correlated to a potentially higher *in situ* production due to more favorable nutrient cycling. Templeton et al. (2021) showed that serpentinized peridotites exhibit a wide range of cell abundances from 10^7 to 10^1 cells g^{-1}, with the highest abundance in the top part of Hole BA1B. Previous studies suggest that continental subsurface bacteria comprise ~21 fg C $cell^{-1}$ (Magnabosco et al., 2018). Using these values, it is possible to calculate the amount of carbon directly derived from cells within the serpentinized peridotites at Site BA. At Hole BA1B, up to $6*10^{-4}$ gC kg^{-1} would be derived from cells, which is <1% of the measured total NCC. These results are consistent with measured ^{14}C ages of NCC, which shows ages from 14 to 3 kyr, suggesting variable sources of carbon and only minor input of modern atmospheric carbon. The incubation experiments of Templeton et al. (2021) showed that, in particular, deeper sections of Hole BA1B are characterized by active microbial sulfate reduction. Combining this observation with the observed trend to younger NCC and TIC with increasing depth at Hole BA1B, we argue that deeper sections are more affected by recent fluid circulation than shallower regions.

The isotopic composition of NCC in the serpentinites from the Wadi Tayin Massif ($\delta^{13}C_{NCC} = -29.6‰$ to $-21.6‰$) differ from the isotopic compositions of organic compounds previously analyzed in well waters from NSHQ04 and NSHQ14 at Site BA ($\delta^{13}C_{CH4,\ short\text{-}chain\ hydrocarbons} = -6.7‰$ to $+6.8‰$, Nothaft, Templeton, Rhim, et al., 2021). Nothaft, Templeton, Rhim, et al. (2021) suggest that a combination of mantle carbon leached from fluid inclusions and microbial activity of methanogens leads to the ^{13}C-enriched compositions of the organic compounds of the well waters. In contrast, the isotopic composition of NCC from the Wadi Tayin Massif is similar to that of serpentinized peridotites from the Atlantis Massif, host of the Lost City hydrothermal field, which ranges from $-28.3‰$ to $-19.8‰$ (Ternieten et al., 2021). Recent rRNA and lipid biomarker analyses of carbonate veins, travertine, and altered peridotites from the Samail Ophiolite (Newman et al., 2020) showed a similar serpentinization microbiome to that of the Lost City hydrothermal field (Bradley et al., 2009; Lincoln et al., 2013; Méhay et al., 2013), including sulfate-reducing and ammonia-oxidizing bacteria, methanogens, and methanotrophs. These results provide evidence supporting the hypothesis of a specific serpentine-inhabiting community occurring in oceanic and continental environments. However, our results cannot distinguish whether microbial production of organic compounds occurs *in situ* or whether they are transported via percolating fluids. In addition, fluid inclusions have been reported previously from the mantle peridotites of the Samail Ophiolite (Miura et al., 2011), and we have to consider leached CH_4 from inclusions as a potential contribution. However, the measurable ^{14}C ages of NCC indicate that mantle carbon is not the sole source of carbon.

To summarize, we suggest a mixture of NCC from microbial activity and minor input from CH_4 leached from fluid inclusions as the main non-carbonate carbon sources in the mantle rocks from the Wadi Tayin Massif. NCC is later removed in the shallow subsurface and dunitic sequence by oxidation from more recent pervasive fluid flow, causing dispersed carbonate formation controlled by micro-fractures that may represent one of the main natural hydraulic plumbing systems within the Samail Ophiolite today.

6. Conclusions

Oman Drilling Project Holes BA1B and BA3A drilled through 400 and 300 m of serpentinized peridotite, respectively, containing several mafic intrusions, fractures, and unconformities. Carbonate occurrences show no record of initial ocean-floor hydration and serpentinization of the Samail Ophiolite. Clumped isotope thermometry of selected veins indicates a carbonation temperature range between 26°C and 43°C, corresponding with mean modern recharge temperatures and post-obduction formation ages of the carbonates. The measured carbon and oxygen isotopes are in part similar to previously investigated carbonates from the Samail Ophiolite but also show distinct characteristics.

We argue that the available data are best explained by a model where focused fluids similar to modern ground- and meteoric water were locally channeled and reacted with the surrounding rock leading to the formation of calcite, dolomite, and aragonite veins in more permeable sections of the ophiolite from ~50 to ~30 kyr. This first phase of carbonization is followed by pervasive infiltration of fluids leading to dispersed carbonate precipitation within the entire Wadi Tayin Massif, yielding a range of ages between 30 kyr and 300 years. Apparent corre-

lations between heterogeneous carbon isotope compositions of the dispersed carbonates and various tectonic features point to infiltration of the reactive fluids at different times and structural levels like fracture planes caused by deformation, micro-fractures from serpentinization, and grain boundaries. Such a model could also explain the highly ^{18}O-depleted composition of the dispersed carbonates. The pervasive nature of the later infiltrating fluid may lead to mixing with low amounts of fossil groundwater with $\delta^{18}O$ values of −7.8‰ (Nicholson et al., 2020). Proportions of mixing may be controlled by the relative access the percolating fluids have to fossil groundwater within the serpentinized peridotites.

These observations also show the importance of a multifaceted approach for creating a conceptual model for heterogeneous alteration and carbonization. Stable oxygen and carbon isotope investigations by themselves can be ambiguous, but including ^{14}C ages of even small amounts of carbon are essential for more realistic constraints on the system and can provide information about the impact of infiltrating fluid. The low amounts of recent carbonate precipitation do not provide evidence for extensive fluid flow within the drilled 300 and 400 m, despite the presence of highly alkaline fluids in the wells (Kelemen et al., 2020), which indicate active serpentinization. Our study suggests that postobduction deformation facilitated repeated advective fluid infiltration into the ophiolite, followed by diffusive transport through the interconnected nano-scale serpentinite pore network that may represent one of the main present-day natural hydraulic plumbing systems within the Samail Ophiolite.

Acknowledgments
The authors would like to thank Madalina Jaggi, Negar Haghipour, Stewart Bishop, and Lydia Zehnder for their help with sample preparation and analyses at ETH. This project was made possible through funding by the International Continental Scientific Drilling Project (ICDP, lead PI's Kelemen, Matter & Teagle), the Alfred P. Sloan Foundation–Deep Carbon Observatory (Grant 2014-3-01, Kelemen PI), the National Science Foundation (NSF-EAR-1516300, Kelemen PI), the NASA Astrobiology Institute (NNA15BB02A, Templeton PI), the German Research Foundation (DFG, Koepke PI), the Japanese Society for the Promotion of Science (JSPS, 16H06347, Michibayashi PI, and 19H00730, Morono PI), the European Research Council (Jamtveit PI), the Swiss National Science Foundation (Früh-Green PI), the Japanese Marine Science and Technology Center (JAMSTEC), the TAMU-JR Science operator, and in-kind contributions from the Sultanate of Oman Ministry of Regional Municipalities and Water Resources, the Oman Public Authority of Mining, Sultan Qaboos University, CRNS- Univ. Montpellier II, Columbia University, and the University of Southampton, and through the efforts of the entire ICDP Expedition 5057 Oman Drilling Project scientific party and support staff from the Oman Drilling Project Science Operator. In particular, the authors thank Jude Coggon, Damon Teagle, and Mazin Al Sulaimani for all their logistical support, Marguerite Goddard and Katsuyoshi Michibayashi for their leadership and in the BA core characterization onboard D/V Chikyu, and Alexis Templeton and her group for providing the MBio sample set and their significant input during inspiring discussions. The authors thank the editor Mark Dekkers and Juan Carlos De Obeso, and Jeffrey Alt for the detailed and constructive reviews that greatly helped improve the manuscript. The authors gratefully acknowledge funding by the Swiss National Science Foundation (SNF) Project no. 200021_163187 and subawards from the Deep Carbon Observatory No. 2019 G VA217 to Früh-Green. Open Access Funding provided by Eidgenossische Technische Hochschule Zurich.

Data Availability Statement

Results of individual analyses are available online on PANGAEA under the following link: https://doi.org/10.1594/PANGAEA.937673.

References

Alt, J. C., & Shanks, W. C. (2003). Serpentinization of abyssal peridotites from the MARK area, Mid-Atlantic Ridge: Sulfur geochemistry and reaction modeling. *Geochimica et Cosmochimica Acta*, *67*(4), 641–653. https://doi.org/10.1016/S0016-7037(02)01142-0

Arai, S., Ishimaru, S., & Mizukami, T. (2012). Methane and propane micro-inclusions in olivine in titanoclinohumite-bearing dunites from the Sanbagawa high-P metamorphic belt, Japan: Hydrocarbon activity in a subduction zone and Ti mobility. *Earth and Planetary Science Letters*, *353*(354), 1–11. https://doi.org/10.1016/j.epsl.2012.07.043

Arvidson, R. S., & Mackenzie, F. T. (1999). The dolomite problem; control of precipitation kinetics by temperature and saturation state. *American Journal of Science*, *299*(4), 257–288. https://doi.org/10.2475/ajs.299.4.257

Auclair, M., Gauthier, M., Trottier, J., Jebrak, M., & Chartrand, F. (1993). Mineralogy, geochemistry, and paragenesis of the Eastern Metals serpentinite-associated Ni-Cu-Zn deposit, Quebec Appalachians. *Economic Geology*, *88*(1), 123–138. https://doi.org/10.2113/gsecongeo.88.1.123

Bach, W., Rosner, M., Jöns, N., Rausch, S., Robinson, L. F., Paulick, H., & Erzinger, J. (2011). Carbonate veins trace seawater circulation during exhumation and uplift of mantle rock: Results from ODP Leg 209. *Earth and Planetary Science Letters*, *311*(3–4), 242–252. https://doi.org/10.1016/j.epsl.2011.09.021

Baker, P. A., & Kastner, M. (1981). Constraints on the formation of sedimentary dolomite. *Science*, *213*(4504), 214 –216. https://doi.org/10.1126/science.213.4504.214

Barnes, I., LaMarche, V. C., & Himmelberg, G. (1967). Geochemical evidence of present-day serpentinization. *Science*, *156*(3776), 830–832. https://doi.org/10.1126/science.156.3776.830

Barnes, I., & O'Neil, J. R. (1969). The relationship between fluids in some fresh alpine-type ultramafics and possible modern serpentinization, Western United StatesTRBFIS]2.0. *Bulletin of the Geological Society of America*, *80*(10), 1947–1960. https://doi.org/10.1130/0016-7606(1969)80

Barnes, I., O'Neil, J. R., Rapp, J. B., & White, D. E. (1973). Silica-carbonate alteration of serpentine: Wall rock alteration in mercury deposits of the California Coast Ranges. *Economic Geology*, *68*(3), 388–398. https://doi.org/10.2113/gsecongeo.68.3.388

Barnes, I., O'Neil, J. R., & Trescases, J. J. (1978). Present day serpentinization in New Caledonia, Oman and Yugoslavia. *Geochimica et Cosmochimica Acta*, *42*(1), 144–145. https://doi.org/10.1016/0016-7037(78)90225-9

Barry, P. H., de Moor, J. M., Giovannelli, D., Schrenk, M. O., Hummer, D. R., Lopez, T., et al. (2019). Forearc carbon sink reduces long-term volatile recycling into the mantle. *Nature*, *568*(7753), 487–492. https://doi.org/10.1038/s41586-019-1131-5

Beinlich, A., John, T., Vrijmoed, J. C., Tominaga, M., Magna, T., & Podladchikov, Y. Y. (2020). Instantaneous rock transformations in the deep crust driven by reactive fluid flow. *Nature Geoscience*, *13*(4), 307–311. https://doi.org/10.1038/s41561-020-0554-9

Beinlich, A., Plümper, O., Boter, E., Müller, I. A., Kourim, F., Ziegler, M., et al. (2020). Ultramafic rock carbonation: Constraints from Listvenite Core BT1B, Oman Drilling Project. *Journal of Geophysical Research: Solid Earth*, *125*(6). https://doi.org/10.1029/2019JB019060

Beinlich, A., Plümper, O., Hövelmann, J., Austrheim, H., & Jamtveit, B. (2012). Massive serpentinite carbonation at Linnajavri, N-Norway. *Terra Nova*, *24*(6), 446–455. https://doi.org/10.1111/j.1365-3121.2012.01083.x

Bernasconi, S. M., Müller, I. A., Bergmann, K. D., Breitenbach, S. F. M., Fernández, Á., Hodell, D. A., et al. (2018). Reducing uncertainties in carbonate clumped isotope analysis through consistent carbonate-based standardization. *Geochemistry, Geophysics, Geosystems*, *19*(9), 2895–2914. https://doi.org/10.1029/2017GC007385

Bjerga, A., Konopásek, J., & Pedersen, R. B. (2015). Talc-carbonate alteration of ultramafic rocks within the Leka Ophiolite Complex, Central Norway. *Lithos*, *227*, 21–36. https://doi.org/10.1016/j.lithos.2015.03.016

Bosak, T., & Newman, D. K. (2003). Microbial nucleation of calcium carbonate in the Precambrian. *Geology*, *31*(7), 577–580. https://doi.org/10.1130/0091-7613(2003)031<0577:MNOCCI>2.0.CO

Boskabadi, A., Pitcairn, I. K., Leybourne, M. I., Teagle, D. A. H., Cooper, M. J., Hadizadeh, H., et al. (2020). Carbonation of ophiolitic ultramafic rocks: Listvenite formation in the Late Cretaceous ophiolites of eastern Iran. *Lithos*, *352–353*, 105307. https://doi.org/10.1016/j.lithos.2019.105307

Boudier, F., & Coleman, R. G. (1981). Cross section through the peridotite in the Samail Ophiolite. *Southeastern Oman Mountains*, *86*(80), 2573–2592.

Bradley, A. S., Hayes, J. M., & Summons, R. E. (2009). Extraordinary ^{13}C enrichment of diether lipids at the Lost City Hydrothermal Field indicates a carbon-limited ecosystem. *Geochimica et Cosmochimica Acta*, *73*(1), 102–118. https://doi.org/10.1016/j.gca.2008.10.005

Brady, P. V., Krumhansl, J. L., & Papenguth, H. W. (1996). Surface complexation clues to dolomite growth. *Geochimica et Cosmochimica Acta*, *60*(4), 727–731. https://doi.org/10.1016/0016-7037(95)00436-X

Braun, M. G. (2004). *Petrologic and microstructural constraints on focused melt transport in dunites and the rheology of the shallow mantle supportive care in cancer*. MIT and Woods Hole Oceanographic Institute. https://doi.org/10.1007/s00520-004-0648-8

Braun, M. G., & Kelemen, P. B. (2002). Dunite distribution in the Oman Ophiolite: Implications for melt flux through porous dunite conduits. *Geochemistry, Geophysics, Geosystems*, *3*(11), 1–21. https://doi.org/10.1029/2001GC000289

Brazelton, W. J., Nelson, B., & Schrenk, M. O. (2012). Metagenomic evidence for H_2 oxidation and H_2 production by serpentinite-hosted subsurface microbial communities. *Frontiers in Microbiology*, *2*, 1–16. https://doi.org/10.3389/fmicb.2011.00268

Breitenbach, S. F. M., & Bernasconi, S. M. (2011). Carbon and oxygen isotope analysis of small carbonate samples (20 to 100 µg) with a GasBench II preparation device. *Rapid Communications in Mass Spectrometry*, *25*(13), 1910–1914. https://doi.org/10.1002/rcm.5052

Bruni, J., Canepa, M., Chiodini, G., Cioni, R., Cipolli, F., Longinelli, A., et al. (2002). Irreversible water-rock mass transfer accompanying the generation of the neutral, Mg–HCO_3 and high-pH, Ca–OH spring waters of the Genova province, Italy. *Applied Geochemistry*, *17*(4), 455–474. https://doi.org/10.1016/S0883-2927(01)00113-5

Cannat, M., Fontaine, F., & Escartín, J. (2010). Serpentinization and associated hydrogen and methane fluxes at slow-spreading ridges. In *Diversity of hydrothermal systems on slow spreading ocean ridges* (pp. 241–264). https://doi.org/10.1029/2008GM000760

Charlou, J. L., Donval, J. P., Fouquet, Y., Jean-Baptiste, P., & Holm, N. G. (2002). Geochemistry of high H_2 and CH_4 vent fluids issuing from ultramafic rocks at the Rainbow hydrothermal field (36°14′N, MAR). *Chemical Geology*, *191*(4), 345–359. https://doi.org/10.1016/S0009-2541(02)00134-1

Chavagnac, V., Monnin, C., Ceuleneer, G., Boulart, C., & Hoareau, G. (2013). Characterization of hyperalkaline fluids produced by low-temperature serpentinization of mantle peridotites in the Oman and Ligurian ophiolites. *Geochemistry, Geophysics, Geosystems*, *14*(7), 2496–2522. https://doi.org/10.1002/ggge.20147

Cipolli, F., Gambardella, B., Marini, L., Ottonello, G., & Zuccolini, M. V. (2004). Geochemistry of high-pH waters from serpentinites of the Gruppo di Voltri (Genova, Italy) and reaction path modeling of CO_2 sequestration in serpentinite aquifers. *Applied Geochemistry*, *19*(5), 787–802. https://doi.org/10.1016/j.apgeochem.2003.10.007

Clark, I. D., & Fontes, J. C. (1990). Paleoclimatic reconstruction in northern Oman based on carbonates from hyperalkaline groundwaters. *Quaternary Research*, *33*(3), 320–336. https://doi.org/10.1016/0033-5894(90)90059-T

Clark, I. D., Fontes, J. C., & Fritz, P. (1992). Stable isotope disequilibria in travertine from high pH waters: Laboratory investigations and field observations from Oman. *Geochimica et Cosmochimica Acta*, *56*(5), 2041–2050. https://doi.org/10.1016/0016-7037(92)90328-G

Coleman, R. G. (1977). Geologic, tectonic, and petrologic nature of four ophiolites. In *Ophiolites: Ancient oceanic lithosphere?* (pp. 159–198). Springer Berlin Heidelberg. https://doi.org/10.1007/978-3-642-66673-5_8

Coleman, R. G. (1981). Tectonic setting for ophiolite obduction in Oman. *Journal of Geophysical Research*, *86*(B4), 2497–2508. https://doi.org/10.1029/JB086iB04p02497

Coleman, R. G., & Hopson, C. A. (1981). Introduction to the Oman ophiolite special issue. *Journal of Geophysical Research: Solid Earth*, *86*(B4), 2495–2496. https://doi.org/10.1029/JB086iB04p02495

Colman, D. R., Poudel, S., Stamps, B. W., Boyd, E. S., & Spear, J. R. (2017). The deep, hot biosphere: Twenty-five years of retrospection. *Proceedings of the National Academy of Sciences of the United States of America*, *114*(27), 6895–6903. https://doi.org/10.1073/pnas.1701266114

Cowan, R. J., Searle, M. P., & Waters, D. J. (2014). Structure of the metamorphic sole to the Oman Ophiolite, Sumeini Window and Wadi Tayyin: Implications for ophiolite obduction processes. *Geological Society Special Publication*, *392*(1), 155–175. https://doi.org/10.1144/SP392.8

Curtis, A. C., Wheat, C. G., Fryer, P., & Moyer, C. L. (2013). Mariana forearc serpentinite mud volcanoes harbor novel communities of extremophilic archaea. *Geomicrobiology Journal*, *30*(5), 430–441. https://doi.org/10.1080/01490451.2012.705226

Daae, F. L., Økland, I., Dahle, H., Jørgensen, S. L., Thorseth, I. H., & Pedersen, R. B. (2013). Microbial life associated with low-temperature alteration of ultramafic rocks in the Leka ophiolite complex. *Geobiology*, *11*(4), 318–339. https://doi.org/10.1111/gbi.12035

de Obeso, J. C., & Kelemen, P. B. (2018). Fluid rock interactions on residual mantle peridotites overlain by shallow oceanic limestones: Insights from Wadi Fins, Sultanate of Oman. *Chemical Geology*, *498*, 139–149. https://doi.org/10.1016/j.chemgeo.2018.09.022

Delacour, A., Früh-Green, G. L., Bernasconi, S. M., & Kelley, D. S. (2008). Sulfur in peridotites and gabbros at Lost City (30°N, MAR): Implications for hydrothermal alteration and microbial activity during serpentinization. *Geochimica et Cosmochimica Acta*, *72*(20), 5090–5110. https://doi.org/10.1016/j.gca.2008.07.017

Delacour, A., Früh-Green, G. L., Bernasconi, S. M., Schaeffer, P., & Kelley, D. S. (2008). Carbon geochemistry of serpentinites in the Lost City Hydrothermal System (30°N, MAR). *Geochimica et Cosmochimica Acta*, *72*(15), 3681–3702. https://doi.org/10.1016/j.gca.2008.04.039

Deppenmeier, U., Müller, V., & Gottschalk, G. (1996). Pathways of energy conservation in methanogenic archaea. *Archives of Microbiology*, *165*(3), 149–163. https://doi.org/10.1007/s002030050310

Dewandel, B., Lachassagne, P., Boudier, F., Al-Hattali, S., Ladouche, B., Pinault, J. L., & Al-Suleimani, Z. (2005). A conceptual hydrogeological model of ophiolite hard-rock aquifers in Oman based on a multiscale and a multidisciplinary approach. *Hydrogeology Journal*, *13*(5–6), 708–726. https://doi.org/10.1007/s10040-005-0449-2

Dick, H. J. B., & Bullen, T. (1984). Chromian spinel as a petrogenetic indicator in abyssal and alpine-type peridotites and spatially associated lavas. *Contributions to Mineralogy and Petrology*, *86*(1), 54–76. https://doi.org/10.1007/BF00373711

Drake, H., Åström, M. E., Heim, C., Broman, C., Åström, J., Whitehouse, M., et al. (2015). Extreme ^{13}C depletion of carbonates formed during oxidation of biogenic methane in fractured granite. *Nature Communications*, *6*(1), 7020. https://doi.org/10.1038/ncomms8020

Dutta, A., Dutta Gupta, S., Gupta, A., Sarkar, J., Roy, S., Mukherjee, A., & Sar, P. (2018). Exploration of deep terrestrial subsurface microbiome in Late Cretaceous Deccan traps and underlying Archean basement, India. *Scientific Reports*, *8*(1), 1–16. https://doi.org/10.1038/s41598-018-35940-0

Etiope, G., & Sherwood Lollar, B. (2013). Abiotic methane on Earth. *Reviews of Geophysics*, *51*(2), 276–299. https://doi.org/10.1002/rog.20011

Falk, E. S., Guo, W., Paukert, A. N., Matter, J. M., Mervine, E. M., & Kelemen, P. B. (2016). Controls on the stable isotope compositions of travertine from hyperalkaline springs in Oman: Insights from clumped isotope measurements. *Geochimica et Cosmochimica Acta*, *192*, 1–28. https://doi.org/10.1016/j.gca.2016.06.026

Falk, E. S., & Kelemen, P. B. (2015). Geochemistry and petrology of listvenite in the Samail ophiolite, Sultanate of Oman: Complete carbonation of peridotite during ophiolite emplacement. *Geochimica et Cosmochimica Acta*, *160*, 70–90. https://doi.org/10.1016/j.gca.2015.03.014

Fernández, Á., Müller, I. A., Rodríguez-Sanz, L., van Dijk, J., Looser, N., & Bernasconi, S. M. (2017). A reassessment of the precision of carbonate clumped isotope measurements: Implications for calibrations and paleoclimate reconstructions. *Geochemistry, Geophysics, Geosystems*, *18*(12), 4375–4386. https://doi.org/10.1002/2017GC007106

Fleitmann, D., Burns, S. J., Pekala, M., Mangini, A., Al-Subbary, A., Al-Aowah, M., et al. (2011). Holocene and Pleistocene pluvial periods in Yemen, Southern Arabia. *Quaternary Science Reviews*, *30*(7–8), 783–787. https://doi.org/10.1016/j.quascirev.2011.01.004

Friedman, I., & O'Neil, J. R. (1977). Compilation of stable isotope fractionation factors of geochemical interest. In *Data of Geochemistry* (6th ed.). U.S. Geological Survey Professional Paper. Retrieved from https://doi.org/10.3133/pp440kk

Frost, R. B., & Beard, J. S. (2007). On silica activity and serpentinization. *Journal of Petrology*, *48*(7), 1351–1368. https://doi.org/10.1093/petrology/egm021

Früh-Green, G. L., Connolly, J. A. D., Plas, A., Kelley, D. S., & Grobéty, B. (2004). Serpentinization of oceanic peridotites: Implications for geochemical cycles and biological activity. In *The subseafloor biosphere at mid-ocean ridges* (pp. 119–136). https://doi.org/10.1029/144GM08

Früh-Green, G. L., Orcutt, B. N., Rouméjon, S., Lilley, M. D., Morono, Y., Cotterill, C., et al. (2018). Magmatism, serpentinization and life: Insights through drilling the Atlantis Massif (IODP Expedition 357). *Lithos*, *323*, 137–155. https://doi.org/10.1016/j.lithos.2018.09.012

Fullerton, K., Schrenk, M. O., Yucel, M., Manini, E., Marco, B., Rogers, T., et al. (2019). Plate tectonics drive deep biosphere microbial community structure. *EarthArXiv*. https://doi.org/10.31223/osf.io/gyr7n

Gartzos, E. (2004). Comparative stable isotopes study of the magnesite deposits of Greece. *Bulletin of the Geological Society of Greece*, *36*(1), 196. https://doi.org/10.12681/bgsg.16619

Gnos, E. (1998). Peak metamorphic conditions of garnet amphibolites beneath the Semail ophiolite: Implications for an inverted pressure gradient. *International Geology Review*, *40*(4), 281–304. https://doi.org/10.1080/00206819809465210

Godard, M., Dautria, J.-M., & Perrin, M. (2003). Geochemical variability of the Oman ophiolite lavas: Relationship with spatial distribution and paleomagnetic directions. *Geochemistry, Geophysics, Geosystems*, *4*(6). https://doi.org/10.1029/2002GC000452

Godard, M., Jousselin, D., & Bodinier, J. L. (2000). Relationships between geochemistry and structure beneath a palaeo-spreading centre: A study of the mantle section in the Oman ophiolite. *Earth and Planetary Science Letters*, *180*(1–2), 133–148. https://doi.org/10.1016/S0012-821X(00)00149-7

Grossman, E. L., & Ku, T. L. (1986). Carbon and oxygen isotopic fractionation in biogenic aragonite-temp effects. *Chemical Geology*, *59*, 59–74.

Hacker, B. R. (1994). Rapid emplacement of young oceanic lithosphere: Argon geochronology of the Oman ophiolite. *Science*, *265*(5178), 1563–1565. https://doi.org/10.1126/science.265.5178.1563

Hacker, B. R., & Gnos, E. (1997). The corundum of Semail: Explaining the metamorphic history. *Tectonophysics*, *279*, 215–226.

Hacker, B. R., & Mosenfelder, J. L. (1996). Metamorphism and deformation along the emplacement thrust of the Samail ophiolite, Oman. *Earth and Planetary Science Letters*, *144*(3–4), 435–451. https://doi.org/10.1016/s0012-821x(96)00186-0

Hacker, B. R., Mosenfelder, J. L., & Gnos, E. (1996). Rapid emplacement of the Oman ophiolite: Thermal and geochronologic constraints. *Tectonics*, *15*(6), 1230–1247.

Halls, C., & Zhao, R. (1995). Listvenite and related rocks: Perspectives on terminology and mineralogy with reference to an occurrence at Creggan baun, Co. Mayo, Republic of Ireland. *Mineral Deposita*, *30*, 303–313.

Hanghoj, K., Kelemen, P. B., Hassler, D., & Godard, M. (2010). Composition and genesis of depleted mantle peridotites from the Wadi Tayin Massif, Oman Ophiolite; Major and trace element geochemistry, and Os isotope and PGE systematics. *Journal of Petrology*, *51*(1–2), 201–227. https://doi.org/10.1093/petrology/egp077

Hopson, C. A., Coleman, R. G., Gregory, R. T., Pallister, J. S., & Bailey, E. H. (1981). Geologic section through the Samail Ophiolite and associated rocks along a Muscat-Ibra Transect, southeastern Oman Mountains. *Journal of Geophysical Research*, *86*(B4), 2527. https://doi.org/10.1029/JB086iB04p02527

Hu, B., Radke, J., Schlüter, H.-J., Heine, F. T., Zhou, L., & Bernasconi, S. M. (2014). A modified procedure for gas-source isotope ratio mass spectrometry: The long-integration dual-inlet (LIDI) methodology and implications for clumped isotope measurements. *Rapid Communications in Mass Spectrometry*, *28*(13), 1413–1425. https://doi.org/10.1002/rcm.6909

Jedrysek, M. O., & Sachanbinski, M. (1994). Stable isotope and trace element studies of vein ophicarbonates at Gogolow-Jordanow serpentinite massif (Poland): A contribution to the origin of ophiaragonite and ophimagnesite. *Geochemical Journal*, *28*(4), 341–350. https://doi.org/10.2343/geochemj.28.341

Katayama, I., Abe, N., Hatakeyama, K., Akamatsu, Y., Okazaki, K., Ulven, O. I., et al. (2020). Permeability profiles across the crust-mantle sections in the Oman drilling project inferred from dry and wet resistivity data. *Journal of Geophysical Research: Solid Earth*, *125*(8), 1–9. https://doi.org/10.1029/2019JB018698

Kelemen, P. B., & Matter, J. M. (2008). In situ carbonation of peridotite for CO_2 storage. *Proceedings of the National Academy of Sciences of the United States of America*, *105*(45), 17295–17300. https://doi.org/10.1073/pnas.0805794105

Kelemen, P. B., Matter, J., Streit, E. E., Rudge, J. F., Curry, W. B., & Blusztajn, J. (2011). Rates and mechanisms of mineral carbonation in peridotite: Natural processes and recipes for enhanced, in-situ CO_2 capture and storage. *Annual Review of Earth and Planetary Sciences*, *39*(1), 545–576. https://doi.org/10.1146/annurev-earth-092010-152509

Kelemen, P. B., Matter, J. M., Teagle, D. A. H., Coggan, J. A., & The Oman Drilling Project Science Team (2020). In P. B. Kelemen, J. M. Matter, D. A. H. Teagle, & J. A. Coggon (Eds.), *Proceedings of the Oman Drilling Project*. International Ocean Discovery Program. https://doi.org/10.14379/OmanDP.proc.2020

Kelemen, P. B., Shimizu, N., & Salters, V. J. M. (1995). Extraction of mid-ocean-ridge basalt from the upwelling mantle by focused flow of melt in dunite channels. *Nature*, *375*(6534), 747–753. https://doi.org/10.1038/375747a0

Kelley, D. S., & Früh-Green, G. L. (2001). Volatile lines of descent in submarine plutonic environments: Insights from stable isotope and fluid inclusion analyses. *Geochimica et Cosmochimica Acta*, *65*(19), 3325–3346. https://doi.org/10.1016/S0016-7037(01)00667-6

Kelley, D. S., Karson, J. A., Früh-Green, G. L., Yoerger, D. R., Shank, T. M., Butterfield, D. A., et al. (2005). A serpentinite-hosted ecosystem: The Lost City hydrothermal field. *Science*, *307*(5714), 1428–1434. https://doi.org/10.1126/science.1102556

Kenward, P. A., Goldstein, R. H., GonzÁlez, L. A., & Roberts, J. A. (2009). Precipitation of low-temperature dolomite from an anaerobic microbial consortium: The role of methanogenic Archaea. *Geobiology*, *7*(5), 556–565. https://doi.org/10.1111/j.1472-4669.2009.00210.x

Konn, C., Charlou, J. L., Holm, N. G., & Mousis, O. (2015). The production of methane, hydrogen, and organic compounds in ultramafic-hosted hydrothermal vents of the mid-atlantic ridge. *Astrobiology*, *15*(5), 381–399. https://doi.org/10.1089/ast.2014.1198

Kourkoumelis, N. (2013). PowDLL, a reusable . NET component for interconverting powder diffraction data: Recent developments. In L. O'Neill (Ed.), *ICDD annual spring meetings* (pp. 137–148).

Labidi, J., Young, E. D., Giunta, T., Kohl, I. E., Seewald, J. S., Tang, H., et al. (2020). Methane thermometry in deep-sea hydrothermal systems: Evidence for re-ordering of doubly-substituted isotopologues during fluid cooling. *Geochimica et Cosmochimica Acta*, *288*. https://doi.org/10.1017/CBO9781107415324.004

Lafuente, B., Downs, R. T., Yang, H., & Stone, N. (2015). The power of databases: The RRUFF project. In T. Armbruster, & R. M. Danisi (Eds.), *Highlights in mineralogical crystallography* (pp. 1–30). De Gruyter. https://doi.org/10.1515/9783110417104-003

Lang, S. Q., Früh-Green, G. L., Bernasconi, S. M., Brazelton, W. J., Schrenk, M. O., & McGonigle, J. M. (2018). Deeply-sourced formate fuels sulfate reducers but not methanogens at Lost City hydrothermal field. *Scientific Reports*, *8*(1), 1–10. https://doi.org/10.1038/s41598-017-19002-5

Lanphere, M. A. (1981). K-Ar ages of metamorphic rocks at the base of the Samail ophiolite, Oman. *Journal of Geophysical Research*, *86*(B4), 2777–2782. https://doi.org/10.1029/JB086iB04p02777

Le Mée, L., Girardeau, J., & Monnier, C. (2004). Mantle segmentation along the Oman ophiolite fossil mid-ocean ridge. *Nature*, *432*(7014), 167–172. https://doi.org/10.1038/nature03075

Li, J., Mara, P., Schubotz, F., Sylvan, J. B., Burgaud, G., Klein, F., et al. (2020). Recycling and metabolic flexibility dictate life in the lower oceanic crust. *Nature*, *579*(7798), 250–255. https://doi.org/10.1038/s41586-020-2075-5

Lincoln, S. A., Bradley, A. S., Newman, S. A., & Summons, R. E. (2013). Archaeal and bacterial glycerol dialkyl glycerol tetraether lipids in chimneys of the Lost City Hydrothermal Field. *Organic Geochemistry*, *60*, 45–53. https://doi.org/10.1016/j.orggeochem.2013.04.010

Lister, C. R. B. (1972). On the thermal balance of a mid-ocean ridge. *Geophysical Journal of the Royal Astronomical Society*, *26*, 515–535.

Magnabosco, C., Lin, L.-H., Dong, H., Bomberg, M., Ghiorse, W., Stan-Lotter, H., et al. (2018). The biomass and biodiversity of the continental subsurface. *Nature Geoscience*, *11*(10), 707–717. https://doi.org/10.1038/s41561-018-0221-6

McCollom, T. M., & Bach, W. (2009). Thermodynamic constraints on hydrogen generation during serpentinization of ultramafic rocks. *Geochimica et Cosmochimica Acta*, *73*(3), 856–875. https://doi.org/10.1016/j.gca.2008.10.032

McCollom, T. M., & Seewald, J. S. (2006). Carbon isotope composition of organic compounds produced by abiotic synthesis under hydrothermal conditions. *Earth and Planetary Science Letters*, *243*(1–2), 74–84. https://doi.org/10.1016/j.epsl.2006.01.027

Meckler, A. N., Ziegler, M., Millán, M. I., Breitenbach, S. F. M., & Bernasconi, S. M. (2014). Long-term performance of the Kiel carbonate device with a new correction scheme for clumped isotope measurements. *Rapid Communications in Mass Spectrometry*, *28*(15), 1705–1715. https://doi.org/10.1002/rcm.6949

Méhay, S., Früh-Green, G. L., Lang, S. Q., Bernasconi, S. M., Brazelton, W. J., Schrenk, M. O., et al. (2013). Record of archaeal activity at the serpentinite-hosted Lost City Hydrothermal Field. *Geobiology*, *11*(6), 570–592. https://doi.org/10.1111/gbi.12062

Menzel, M. D., Garrido, C. J., López Sánchez-Vizcaíno, V., Marchesi, C., Hidas, K., Escayola, M. P., & Delgado Huertas, A. (2018). Carbonation of mantle peridotite by CO_2-rich fluids: The formation of listvenites in the Advocate ophiolite complex (Newfoundland, Canada). *Lithos*, *323*, 238–261. https://doi.org/10.1016/j.lithos.2018.06.001

Mervine, E. M., Humphris, S. E., Sims, K. W. W., Kelemen, P. B., & Jenkins, W. J. (2014). Carbonation rates of peridotite in the Samail Ophiolite, Sultanate of Oman, constrained through ^{14}C dating and stable isotopes. *Geochimica et Cosmochimica Acta*, *126*, 371–397. https://doi.org/10.1016/j.gca.2013.11.007

Miller, H. M., Matter, J. M., Kelemen, P. B., Ellison, E. T., Conrad, M. E., Fierer, N., et al. (2016). Modern water/rock reactions in Oman hyperalkaline peridotite aquifers and implications for microbial habitability. *Geochimica et Cosmochimica Acta*, *179*, 217–241. https://doi.org/10.1016/j.gca.2016.01.033

Miura, M., Arai, S., & Mizukami, T. (2011). Raman spectroscopy of hydrous inclusions in olivine and orthopyroxene in ophiolitic harzburgite: Implications for elementary processes in serpentinization. *Journal of Mineralogical and Petrological Sciences*, *106*(2), 91–96. https://doi.org/10.2465/jmps.101021d

Monnier, C., Girardeau, J., Le Mée, L., & Polvé, M. (2006). Along-ridge petrological segmentation of the mantle in the Oman ophiolite. *Geochemistry, Geophysics, Geosystems*, *7*(11). https://doi.org/10.1029/2006GC001320

Moore, T. S., Murray, R. W., Kurtz, A. C., & Schrag, D. P. (2004). Anaerobic methane oxidation and the formation of dolomite. *Earth and Planetary Science Letters*, *229*(1–2), 141–154. https://doi.org/10.1016/j.epsl.2004.10.015

Moreira, N. F., Walter, L. M., Vasconcelos, C., McKenzie, J. A., & McCall, P. J. (2004). Role of sulfide oxidation in dolomitization: Sediment and pore-water geochemistry of a modern hypersaline lagoon system. *Geology*, *32*(8), 701. https://doi.org/10.1130/G20353.1

Mottl, M. J., Komor, S. C., Fryer, P., & Moyer, C. L. (2003). Deep-slab fluids fuel extremophilic Archaea on a Mariana forearc serpentinite mud volcano: Ocean drilling program leg 195. *Geochemistry, Geophysics, Geosystems*, *4*(11), 1–14. https://doi.org/10.1029/2003GC000588

Müller, I. A., Fernández, Á., Radke, J., van Dijk, J., Bowen, D., Schwieters, J., & Bernasconi, S. M. (2017). Carbonate clumped isotope analyses with the long-integration dual-inlet (LIDI) workflow: Scratching at the lower sample weight boundaries. *Rapid Communications in Mass Spectrometry*, *31*(12), 1057–1066. https://doi.org/10.1002/rcm.7878

Müller, I. A., Rodriguez-Blanco, J. D., Storck, J.-C., do Nascimento, G. S., Bontognali, T. R. R., Vasconcelos, C., et al. (2019). Calibration of the oxygen and clumped isotope thermometers for (proto-) dolomite based on synthetic and natural carbonates. *Chemical Geology*, *525*, 1–17. https://doi.org/10.1016/j.chemgeo.2019.07.014

Müller, I. A., Violay, M. E. S., Storck, J.-C., Fernández, Á., van Dijk, J., Madonna, C., & Bernasconi, S. M. (2017). Clumped isotope fractionation during phosphoric acid digestion of carbonates at 70°C. *Chemical Geology*, *449*, 1–14. https://doi.org/10.1016/j.chemgeo.2016.11.030

Nasir, S., Al Sayigh, A. R., Al Harthy, A., Al-Khirbash, S., Al-Jaaidi, O., Musllam, A., et al. (2007). Mineralogical and geochemical characterization of listwaenite from the Semail Ophiolite, Oman. *Chemie der Erde*, *67*(3), 213–228. https://doi.org/10.1016/j.chemer.2005.01.003

Neal, C., & Stanger, G. (1983). Hydrogen generation from mantle source rocks in Oman. *Earth and Planetary Science Letters*, *66*(C), 315–320. https://doi.org/10.1016/0012-821X(83)90144-9

Neal, C., & Stanger, G. (1985). Past and present serpentinisation of ultramafic rocks; An example from the Semail Ophiolite Nappe of Northern Oman BT – The chemistry of weathering. In J. I. Drever (Ed.), (pp. 249–275). Springer Netherlands. https://doi.org/10.1007/978-94-009-5333-8_15

Newman, S. A., Lincoln, S. A., O'Reilly, S., Liu, X., Shock, E. L., Kelemen, P. B., & Summons, R. E. (2020). Lipid biomarker record of the serpentinite-hosted ecosystem of the Samail Ophiolite, Oman and implications for the search for biosignatures on Mars. *Astrobiology*, *20*(7), 830–845. https://doi.org/10.1089/ast.2019.2066

Nicholson, S. L., Pike, A. W. G., Hosfield, R., Roberts, N., Sahy, D., Woodhead, J., et al. (2020). Pluvial periods in Southern Arabia over the last 1.1 million-years. *Quaternary Science Reviews*, *229*. https://doi.org/10.1016/j.quascirev.2019.106112

Nicolas, A. (1989). *Structures of ophiolites and dynamics of oceanic lithosphere*. Springer Netherlands. https://doi.org/10.1007/978-94-009-2374-4

Nicolas, A., Boudier, F., Ildefonse, B., & Ball, E. (2000). Accretion of Oman and United Arab Emirates ophiolite – Discussion of a new structural map. *Marine Geophysical Researches*, *21*(3/4), 147–180. https://doi.org/10.1023/A:1026769727917

Noël, J., Godard, M., Oliot, E., Martinez, I., Williams, M. J., Boudier, F., et al. (2018). Evidence of polygenetic carbon trapping in the Oman Ophiolite: Petro-structural, geochemical, and carbon and oxygen isotope study of the Wadi Dima harzburgite-hosted carbonates (Wadi Tayin massif, Sultanate of Oman). *Lithos*, *323*, 218–237. https://doi.org/10.1016/j.lithos.2018.08.020

Nothaft, D. B., Templeton, A. S., Boyd, E. S., Matter, J. M., Stute, M., & Paukert Vankeuren, A. N. (2021). Aqueous geochemical and microbial variation across discrete depth intervals in a peridotite aquifer assessed using a packer system in the Samail Ophiolite, Oman. *Journal of Geophysical Research: Biogeosciences*, *126*(9). https://doi.org/10.1029/2021JG006319

Nothaft, D. B., Templeton, A. S., Rhim, J. H., Wang, D. T., Labidi, J., Miller, H. M., et al. (2021). Geochemical, biological, and clumped isotopologue evidence for substantial microbial methane production under carbon limitation in serpentinites of the Samail Ophiolite, Oman. *Journal of Geophysical Research: Biogeosciences*, *126*(10), 1–30. https://doi.org/10.1029/2020jg006025

Ohara, Y., Reagan, M. K., Fujikura, K., Watanabe, H., Michibayashi, K., Ishii, T., et al. (2012). A serpentinite-hosted ecosystem in the Southern Mariana Forearc. *Proceedings of the National Academy of Sciences of the United States of America*, *109*(8), 2831–2835. https://doi.org/10.1073/pnas.1112005109

O'Neil, J. R., & Barnes, I. (1971). C_{13} and O_{18} compositions in some fresh-water carbonates associated with ultramafic rocks and serpentinites: Western United States. *Geochimica et Cosmochimica Acta*, *35*(7), 687–697. https://doi.org/10.1016/0016-7037(71)90067-6

O'Neil, J. R., Clayton, R. N., & Mayeda, T. K. (1969). Oxygen isotope fractionation in divalent metal carbonates. *The Journal of Chemical Physics*, *51*(12), 5547–5558. https://doi.org/10.1063/1.1671982

Orcutt, B. N., Bergenthal, M., Freudenthal, T., Smith, D., Lilley, M. D., Schnieders, L., et al. (2017). Contamination tracer testing with seabed drills: IODP Expedition 357. *Scientific Drilling*, *23*, 39–46. https://doi.org/10.5194/sd-23-39-2017

Palandri, J. L., & Reed, M. H. (2004). Geochemical models of metasomatism in ultramafic systems: Serpentinization, rodingitization, and sea floor carbonate chimney precipitation. *Geochimica et Cosmochimica Acta*, *68*(5), 1115–1133. https://doi.org/10.1016/j.gca.2003.08.006

Pallister, J. S., & Knight, R. J. (1981). Rare-Earth Geochemistry of the Samail Ophiolite near Ibra, Oman. *Journal of Geophysical Research*, *86*(80), 2673–2697.

Paukert, A. N., Matter, J. M., Kelemen, P. B., Shock, E. L., & Havig, J. R. (2012). Reaction path modeling of enhanced in situ CO_2 mineralization for carbon sequestration in the peridotite of the Samail Ophiolite, Sultanate of Oman. *Chemical Geology*, *330–331*, 86–100. https://doi.org/10.1016/j.chemgeo.2012.08.013

Paukert Vankeuren, A. N., Matter, J. M., Stute, M., & Kelemen, P. B. (2019). Multitracer determination of apparent groundwater ages in peridotite aquifers within the Samail ophiolite, Sultanate of Oman. *Earth and Planetary Science Letters*, *516*, 37–48. https://doi.org/10.1016/j.epsl.2019.03.007

Pedersen, K., Ekendahl, S., Tullborg, E.-L., Furnes, H., Thorseth, I., & Tumyr, O. (1997). Evidence of ancient life at 207 m depth in a granitic aquifer. *Geology*, *25*(9), 827. https://doi.org/10.1130/0091-7613(1997)025<0827:EOALAM>2.3.CO;2

Quesnel, B., Boulvais, P., Gautier, P., Cathelineau, M., John, C. M., Dierick, M., et al. (2016). Paired stable isotopes (O, C) and clumped isotope thermometry of magnesite and silica veins in the New Caledonia Peridotite Nappe. *Geochimica et Cosmochimica Acta*, *183*, 234–249. https://doi.org/10.1016/j.gca.2016.03.021

Quesnel, B., Gautier, P., Boulvais, P., Cathelineau, M., Maurizot, P., Cluzel, D., et al. (2013). Syn-tectonic, meteoric water-derived carbonation of the New Caledonia peridotite nappe. *Geology*, *41*(10), 1063–1066. https://doi.org/10.1130/G34531.1

Rabu, D., Nehlig, P., Roger, J., Béchennec, F., Beurrier, M., Le Métour, J., et al. (1993). *Stratigraphy and structure of the Oman mountains*.

Ravaut, P., Bayer, R., Hassani, R., Rousset, D., & Al Yahya'Ey, A. (1997). Structure and evolution of the northern Oman margin: Gravity and seismic constraints over the Zagros-Makran-Oman collision zone. *Tectonophysics*, *279*(1–4), 253–262. https://doi.org/10.1016/S0040-1951(97)00125-X

Reimer, P. J., Brown, T. A., & ReimerRon, W. (2004). Discussion: Reporting and calibration of post-bomb 14C data. *Radiocarbon*, *46*(1), 1111–1150.

Rioux, M., Bowring, S. A., Kelemen, P. B., Gordon, S., Dudás, F., & Miller, R. (2012). Rapid crustal accretion and magma assimilation in the Oman-U.A.E. ophiolite: High precision U-Pb zircon geochronology of the gabbroic crust. *Journal of Geophysical Research: Solid Earth*, *117*(B7). https://doi.org/10.1029/2012JB009273

Rioux, M., Bowring, S. A., Kelemen, P. B., Gordon, S., Miller, R., & Dudás, F. (2013). Tectonic development of the Samail ophiolite: High-precision U-Pb zircon geochronology and Sm-Nd isotopic constraints on crustal growth and emplacement. *Journal of Geophysical Research*, *118*(5), 2085–2101. https://doi.org/10.1002/jgrb.50139

Rioux, M., Garber, J., Bauer, A., Bowring, S. A., Searle, M. P., Kelemen, P. B., & Hacker, B. R. (2016). Synchronous formation of the metamorphic sole and igneous crust of the Semail ophiolite: New constraints on the tectonic evolution during ophiolite formation from high-precision U–Pb zircon geochronology. *Earth and Planetary Science Letters*, *451*, 185–195. https://doi.org/10.1016/j.epsl.2016.06.051

Rozanski, K., Araguás-Araguás, L., & Gonfiantini, R. (1993). Isotopic patterns in modern global precipitation. *Climate change in continental isotopic records, geophysical monograph* (pp. 1–36). American Geophysical Union. https://doi.org/10.1029/GM078p0001

Ruff, M., Szidat, S., Gäggeler, H. W., Suter, M., Synal, H. A., & Wacker, L. (2010). Gaseous radiocarbon measurements of small samples. *Nuclear Instruments and Methods in Physics Research Section B: Beam Interactions with Materials and Atoms*, *268*(7–8), 790–794. https://doi.org/10.1016/j.nimb.2009.10.032

Sánchez-Román, M., McKenzie, J. A., de Luca Rebello Wagener, A., Rivadeneyra, M. A., & Vasconcelos, C. (2009). Presence of sulfate does not inhibit low-temperature dolomite precipitation. *Earth and Planetary Science Letters*, *285*(1–2), 131–139. https://doi.org/10.1016/j.epsl.2009.06.003

Schrenk, M. O., Brazelton, W. J., & Lang, S. Q. (2013). Serpentinization, carbon, and deep life. *Reviews in Mineralogy and Geochemistry*, *75*, 575–606. https://doi.org/10.2138/rmg.2013.75.18

Schroeder, T. J., Bach, W., Jöns, N., Jöns, S., Monien, P., & Klügel, A. (2015). Fluid circulation and carbonate vein precipitation in the footwall of an oceanic core complex, Ocean Drilling Program Site 175, Mid-Atlantic Ridge. *Geochemistry, Geophysics, Geosystems*, *16*(10), 3716–3732. https://doi.org/10.1002/2015GC006041

Schwarzenbach, E. M., Früh-Green, G. L., Bernasconi, S. M., Alt, J. C., & Plas, A. (2013a). Serpentinization and carbon sequestration: A study of two ancient peridotite-hosted hydrothermal systems. *Chemical Geology*, *351*, 115–133. https://doi.org/10.1016/j.chemgeo.2013.05.016

Schwarzenbach, E. M., Lang, S. Q., Früh-Green, G. L., Lilley, M. D., Bernasconi, S. M., & Méhay, S. (2013b). Sources and cycling of carbon in continental, serpentinite-hosted alkaline springs in the Voltri Massif, Italy. *Lithos*, *177*, 226–244. https://doi.org/10.1016/j.lithos.2013.07.009

Scicchitano, M. R., Spicuzza, M. J., Ellison, E. T., Tuschel, D., Templeton, A. S., & Valley, J. W. (2020). In situ oxygen isotope determination in serpentine minerals by SIMS: Addressing matrix effects and providing new insights on serpentinisation at hole BA1B (Samail ophiolite, Oman). *Geostandards and Geoanalytical Research*. *45*(1), 12359. https://doi.org/10.1111/ggr.12359

Searle, M. P., & Malpas, J. (1980). Structure and metamorphism of rocks beneath the Semail ophiolite of Oman and their significance in ophiolite obduction. *Transactions of the Royal Society of Edinburgh Earth Sciences*, *71*(4), 247–262. https://doi.org/10.1017/S0263593300013614

Searle, M. P., Waters, D. J., Garber, J., Rioux, M., Cherry, A. G., & Ambrose, T. K. (2015). Structure and metamorphism beneath the obducting Oman ophiolite: Evidence from the Bani Hamid granulites, northern Oman Mountains. *Geosphere*, *11*(6), 1812–1836. https://doi.org/10.1130/GES01199.1

Shanks, W. C., Böhlke, J. K., & Seal, R. R. (1995). Stable isotopes in mid-ocean ridge hydrothermal systems: Interactions between fluids, minerals, and organisms. *SeaBoor Hydrothermal Systems: Physical, Chemical, Biological, and Geological Interactions*, *70*, 194–221.

Sibley, D. F., Dedoes, R. E., & Bartlett, T. R. (1987). Kinetics of dolomitization. *Geology*, *15*(12), 11122. https://doi.org/10.1130/0091-7613(1987)15<1112:KOD>2.0

Stanger, G. (1985). Silicified serpentinite in the Semail nappe of Oman. *Lithos*, *18*(C), 13–22. https://doi.org/10.1016/0024-4937(85)90003-9

Streit, E. E., Kelemen, P. B., & Eiler, J. M. (2012). Coexisting serpentine and quartz from carbonate-bearing serpentinized peridotite in the Samail Ophiolite, Oman. *Contributions to Mineralogy and Petrology*, *164*(5), 821–837. https://doi.org/10.1007/s00410-012-0775-z

Synal, H. A., Stocker, M., & Suter, M. (2007). MICADAS: A new compact radiocarbon AMS system. *Nuclear Instruments and Methods in Physics Research Section B: Beam Interactions with Materials and Atoms*, *259*(1), 7–13. https://doi.org/10.1016/j.nimb.2007.01.138

Templeton, A. S., Ellison, E. T., Glombitza, C., Morono, Y., Rempfert, K. R., Hoehler, T. M., et al. (2021). Accessing the subsurface biosphere within rocks undergoing active low-temperature serpentinization in the Samail Ophiolite (Oman Drilling Project). *Journal of Geophysical Research: Biogeosciences*, *126*(10). https://doi.org/10.1029/2021jg006315

Ternieten, L., Früh-Green, G. L., & Bernasconi, S. M. (2021). Distribution and sources of carbon in serpentinized mantle peridotites at the Atlantis Massif (IODP Expedition 357). *Journal of Geophysical Research: Solid Earth*, *126*(10). https://doi.org/10.1029/2021jb021973

Tilton, G. R., Hopson, C. A., & Wright, J. E. (1981). Uranium-lead isotopic ages of the Samail ophiolite, Oman, with applications to Tethyan ocean ridge tectonics. *Journal of Geophysical Research*, *86*(B4), 2763–2775. https://doi.org/10.1029/JB086iB04p02763

Vasconcelos, C., Mckenzie, J. A., Bernasconi, S., Grujic, D., & Tien, A. J. (1995). Microbial mediation as a possible mechanism for natural dolomite formation at low temperatures. *Nature*, *377*, 220–222.

Wacker, L., Bonani, G., Friedrich, M., Hajdas, I., Kromer, B., Němec, M., et al. (2010). Micadas: Routine and high-precision radiocarbon dating. *Radiocarbon*, *52*(2), 252–262. https://doi.org/10.1017/S0033822200045288

Wang, D. T., Reeves, E. P., McDermott, J. M., Seewald, J. S., & Ono, S. (2018). Clumped isotopologue constraints on the origin of methane at seafloor hot springs. *Geochimica et Cosmochimica Acta*, *223*, 141–158. https://doi.org/10.1016/j.gca.2017.11.030

Warren, C. J., Parrish, R. R., Waters, D. J., & Searle, M. P. (2005). Dating the geologic history of Oman's Semail ophiolite: Insights from U-Pb geochronology. *Contributions to Mineralogy and Petrology*, *150*(4), 403–422. https://doi.org/10.1007/s00410-005-0028-5

Wheat, C. G., & Mottl, M. J. (2004). Geochemical fluxes through mid-ocean ridge flanks. In *Hydrogeology of the oceanic lithosphere* (pp. 627–658).

Zeebe, R. E. (2020). Oxygen isotope fractionation between water and the aqueous hydroxide ion. *Geochimica et Cosmochimica Acta*, *289*, 182–195. https://doi.org/10.1016/j.gca.2020.08.025